Short-term fluctuations south of Japan and their relationship with the Kuroshio path: 8- to 36-day fluctuations

Ocean Dynamics, *in press*

Toru Miyama[1] and Yasumasa Miyazawa[1],

1. Research Institute for Global Change, Japan Agency for Marine-Earth Science and Technology, Yokohama, Japan

Corresponding Author:

Toru Miyama,

Research Institute for Global Change, Japan Agency for Marine-Earth Science and Technology, 3173-25 Showamachi, Kanazawa-ku, Yokohama, 236-0001, Japan

tmiyama@jamstec.go.jp TEL : +81-45-778-5700 FAX : +81-45-778-5497

Abstract

To detect short-term fluctuations south of Japan, we applied wavelet analysis to ocean-reanalysis data of the Japan Coastal Ocean Predictability Experiment 2 (JCOPE2) with a horizontal resolution of 1/36º. It was found that fluctuations of the 8- to 36-day period band appear as frontal waves in the Kuroshio Current. The amplitude of the fluctuations increases toward the downstream of Cape Shionomisaki. The fluctuations have a wavelength of about 300 km, and the signals propagate eastward. The fluctuations of the 8- to 36-day period band are stronger during the period of the nearshore non-large-meander Kuroshio path than during the period of the offshore non-large-meander Kuroshio path. We suggest that the 8- to 36-day fluctuation is a result of the instability of the accelerated velocity of the Kuroshio Current downstream of Cape Shionomisaki.

Keywords: Kuroshio path, short-term fluctuation, instability, frontal wave, wavelet, ocean reanalysis

1. Introduction

The fluctuations of the strong Kuroshio Current, which flows near the southern coast of Japan, strongly affect the coastal environment. The region discussed in this paper (Fig. 1) is a unique location where the Kuroshio path changes with time dramatically (Kawabe 1985). The Kuroshio has bimodal paths: a large-meander path and a non-large-meander path. The non-large-meander path is further classified into a nearshore non-large-meander path and an offshore non-large-meander path, which are schematically shown in Fig. 1. While the Kuroshio large-meander occurs with a primary period of about 20 years and secondary period of 7 to 8.5 years, the switch between the nearshore and offshore paths happens with a primary period of 1.6-1.8 years along with 110-day, 195-day and annual periods (Kawabe 1987).

In addition to these path shifts, there are active short-term fluctuations off the southern coast of Japan. In this paper, short-term fluctuation means fluctuations of periods less than 80 days. Past studies have reported the existence of fluctuations of roughly 10- to 30-day period (Taft 1978; Taira and Teramoto 1981; Kimura and Sugimoto 1987; Kasai et al. 1993; Kimura and Sugimoto 1993; Ramp et al. 2008). The fluctuations of this period appear as frontal waves of the Kuroshio. From hydrographic data, Taft (1978) found an eastward propagating wave having a wavelength of 330 km and a phase speed of 0.14 m/s. From velocity observations off Cape Shionomisaki, Kimura and Sugimoto (1993) estimated dominant periods of 5–8 days, 10–12 days, and 17–19 days with wavelengths of 100, 200, and 400 km,

53 respectively. The frontal waves stimulate exchange between coastal waters off the southern coast of
54 Japan and the waters of the Kuroshio. Because of the water exchange, the short-term fluctuations affect
55 the supply of nutrients (Kimura et al. 1997), primary production (Kimura et al. 1997; Ramp et al. 2008),
56 and fishery conditions (Kimura and Sugimoto 1987; Kasai et al. 2002; Waseda and Mitsudera 2002;
57 Okazaki et al. 2003). A fluctuation of a period of around 50- to 70-day, which is another fluctuation, is
58 related to the S-shaped meandering pattern of the Kuroshio around the Izu Ridge (Kasai et al. 1993;
59 Mitsudera et al. 2006; Takahashi et al. 2011).

60 Some studies have shown that the periodicities of short-term fluctuations changed with the Kuroshio
61 path. Takahashi et al. (2011) found that a period of less than 40 days became weak in Sagami Bay after
62 the transition from a nearshore non-large-meander path to an offshore non-large-meander-path around
63 June 3, 2008. Instead, fluctuations of 50- to 70-day periods became dominant. This is consistent with the
64 observation by Kasai et al. (1993) in that fluctuations of a 50-day period were dominant only when the
65 Kuroshio took an offshore non-large-meander path.

66 Past observations of short-term fluctuations have been conducted in limited locations and periods.
67 Therefore, descriptions of short-term fluctuations in the Kuroshio are intermittent. Satellite data of sea
68 surface temperature (SST) and sea surface heights (SSH), which have good spatial coverage, have been
69 used in studies on short-term fluctuations (Kasai et al. 1993; Kimura et al. 1997; Takahashi et al. 2011;
70 Takahashi et al. 2012). Obtaining SST images from satellites, however, is often hampered by clouds.

71 Since SSH observations by satellite altimeters usually have a 7- to 10-day time-resolution, it is difficult
72 to capture fluctuations of 10- to 30-day periods. On the other hand, ocean assimilation data can
73 compensate for missing observational data in space and time with the help of a numerical model. The
74 main objective of this study is to describe the short-term fluctuations of the Kuroshio using an ocean
75 assimilation dataset, the Japan Coastal Ocean Predictability Experiment 2 (JCOPE2) reanalysis. We are
76 particularly interested in how the short-term fluctuation responds to shifts in the Kuroshio path with time.
77 Among the Kuroshio paths, we investigate the shifts between the nearshore and offshore
78 non-large-meander paths.
79 We aim to determine not only the distribution of the fluctuations, but also the time fluctuations of
80 these distributions. Therefore, we used a wavelet analysis, which provides information regarding the
81 amplitude of periodic signals from a time series and the fluctuation of the amplitude with time. Because
82 past studies have identified two types of fluctuations, 10- to 30-day and 50 to 70-day fluctuations, we
83 classified the fluctuations into bands of 8- to 36-days and 40- to 80-days. Section 2 describes how we
84 selected these bands. In this paper, we particularly address the 8- to 36-day fluctuations.
85 This paper is organized as follows. In Section 2, we introduce the data used in this study, i.e., the
86 JCOPE2 reanalysis dataset. In addition, we explain the wavelet analysis used to describe short-term
87 fluctuations. In Section 3, we show the distribution of the fluctuations and its relationship with the
88 Kuroshio path. In Section 4, we describe typical structures of the 8- to 36-day fluctuations. In section 5,

89 we show the vertical structure. In Section 6, we investigate the relationship of the fluctuations with the
90 Kuroshio velocity. In Section 7, we summarize and discuss the results.
91
92 ## 2. Data and Methods
93 ### 2.1 Data
94 The ocean reanalysis data used in this study is a product of the JCOPE2 (Miyazawa et al. 2009). This
95 dataset has a horizontal resolution of 1/36°, 46 vertical levels, and covers the area 28°N–36°N,
96 128°E–142°E. In this paper, we particularly discuss the region from around Cape Shionomisaki to
97 around the Izu Ridge (135–140°E; Fig. 1). The lateral boundary conditions were determined from the
98 standard JCOPE2 reanalysis (Miyazawa et al. 2009) using a one-way nesting method with a flow
99 relaxation scheme (Oey and Chen 1992; Guo et al. 2003).
100 The dataset in this study is a revised version of that used in Miyama and Miyazawa (2013). While the
101 model used in Miyama and Miyazawa (2013) was forced by the wind stress and heat flux fields of the
102 6-hourly National Centers for Environmental Prediction/National Center for Atmospheric Research
103 (NCEP/NCAR) reanalysis data (2.5°×2.5° horizontal resolution; Kalnay et al. 1996), the reanalysis used
104 in this study was forced by the 3-hourly data of the Japan Meteorological Agency Meso Scale Model
105 analysis (MSM; 0.125°×0.1° horizontal resolution; Saito et al. 2007). The available dataset in this study
106 includes daily-mean data, spanning about five and a quarter years (February 23, 2006 to May 31, 2011),

which is longer than the roughly four and half years (August 2003 to December 2007) of the dataset used by Miyama and Miyazawa (2013). Note that the dataset used in this study does not include the large-meander period from the second half of 2004 to the first half of 2005 (Miyazawa et al. 2008). Therefore, we discuss the short-term fluctuations during the periods of the nearshore non-large-meander and the offshore non-large-meander paths of the Kuroshio. Hereafter, we simply refer to these paths as the nearshore and the offshore paths, omitting the term "non-large-meander". We can better analyze the short-term fluctuations in these nearshore and offshore paths from the longer data period (more than five years) than from the period in the data used by Miyama and Miyazawa (2013). We cannot use the whole period of the data in Miyama and Miyazawa (2013) continuously because of about one year of the large-meander path from the second half of 2004 to the first half of 2005, which was a state dynamically different form the rest of the period. The overlapping period between data used in this study and that in Miyama and Miyazawa (2013) shows qualitatively the same results (not shown).

2.2 Wavelet analysis

We used the continuous wavelet analysis described in Torrence and Compo (1998). Examples of the wavelet analysis results are presented in Figs. 2 to 4. Figure 2a shows the time series for SSH at 139ºE, 33.25ºN, and Figure 2b shows the normalized wavelet power spectrum of this time series using the Morlet wavelet. There are significant short-term fluctuations in the wavelet power spectrum in periods of less than 80 days.

125 By averaging the wavelet spectrum over the whole time period (Section 5a of Torrence and Compo
126 1998), we can obtain the global wavelet power spectrum (solid line in Fig. 3). Figure 3 confirms that the
127 short-term fluctuations are significant: the global power spectrum (solid line) is above the 95%
128 confidence level (dashed line). There are two peaks in the global spectrum: between 8 and 36 days and
129 between 40 and 80 days. The existence of the two peaks is consistent with the past observations that
130 there are two kinds of short-term fluctuations of periods of about 20 days and 50 days (Kasai et al. 1993).
131 From Fig. 3 and from similar results at other points (not shown), we classified the short-term
132 fluctuations into 8- to 36-day fluctuations and 40- to 80-day fluctuations. However, we only discuss the
133 8- to 36-day fluctuations in this paper, except short descriptions on 40- to 80-day fluctuations in
134 Appendix A.
135 Although some studies have detected fluctuations of around a 10-day period in addition to the
136 fluctuations of 20- to 30-day period (Kimura and Sugimoto 1993; Hinata et al. 2008; Ramp et al. 2008),
137 we did not treat these period bands separately because we found it difficult to differentiate their peaks in
138 this analysis. For further discussion regarding this, see Section 7. Some studies (Kimura and Sugimoto
139 1993; Kimura et al. 1994; Ramp et al. 2008) found fluctuations of a period of a few days. Because
140 analyzing periods less than 8 days is difficult when using daily data, we analyzed periods more than 8
141 days.
142 By averaging the wavelet power spectrum in Fig.2b over a certain period band, we can obtain a time

143 series of the averaged variance (m^2) (Section 5*b* of Torrence and Compo (1998)). The solid red lines in
144 Fig. 4 is the time series of averaged variance over 8- to 36-day. In this paper, the period-averaged power
145 spectrum is referred to as the "variance" of the corresponding period band.
146 It is also possible to reconstruct the original time series inversely from the wavelet coefficients
147 (Section 3*i* of Torrence and Compo (1998)). By using the wavelet coefficients in a certain period band,
148 we can reconstruct the time series of SSH fluctuations (in meters) in the corresponding period band. The
149 solid black line in Fig. 4 is the reconstructed time series using the wavelet coefficients in the 8- to
150 36-day period band. This is equivalent to the 8- to 36-day band-pass-filtered time series of the original
151 time series (Fig. 2a). In this paper, the band-pass-filtered fluctuation of the original time series using the
152 wavelet method is referred to as the "signal" of the period band.
153 Throughout this paper, we use the method described above to obtain the variance and signal of the 8-
154 to 36-day periods from the original time series in the region shown in Fig. 1. Among the available data in
155 the JCOPE2 reanalysis, we start with the wavelet analysis for SSH, which reflects the ocean dynamics
156 beneath the surface. Later in the discussion, we use velocity, temperature, and salinity (for density) data.
157 Although we applied the wavelet analysis to the data of the whole time period (from Feb. 23, 2006 to
158 May 31, 2011), we only describe the data from April 15, 2006 to April 14, 2011 in order to minimize the
159 influence of the data edges (indicated by the cross-hatched regions in Fig. 2b).
160

3. Horizontal distribution and its relation to the Kuroshio path

In this section, we describe the horizontal distribution of the 8- to 36-day fluctuations. The color shading in Fig. 5 shows the horizontal maps of variances of the 8- to 36-day period band, time-averaged over the whole analysis time period (from April 15, 2006 to April 14, 2011). This figure was obtained by applying the wavelet analysis at every model grid point. The contours in Fig. 5 show the unfiltered SSH time-averaged over the same period. By geostrophy, the contours indicate the direction of flow of ocean currents, and the narrow spacing between the lines indicates strong Kuroshio flow in this region. The 8- to 36-day fluctuations are active in the region where the Kuroshio flows. A high variance spreads from east to west between 33º and 34ºN. The relatively low variance near Cape Shionomisaki is amplified toward the high variance around the area west of the Izu ridge.

In order to study how short-term fluctuations respond to shifts in the Kuroshio path, we first define the Kuroshio path. Looking at the relationship between the surface velocity and SSH in the JCOPE2 reanalysis, we found that the SSH isoline of 0.1 m is located around the maximum of the surface velocity (not shown). Therefore, we define the the SSH isoline of 0.1 m as the Kuroshio path. Similar definitions using SSH isolines were used by Qiu and Chen (2005) and Sugimoto and Hanawa (2011). Because we are interested in the response of the short-term fluctuations to the low-frequency change of the background flow, we used a low-pass-filtered SSH to define the Kuroshio path. We again used the wavelet method, and obtained a 90-day low-pass-filtered signal of SSH by reconstructing the signal

179 from the wavelet coefficients for periods longer than 90 days.

180 After defining the Kuroshio path from the low-pass-filtered SSH, the distance of the Kuroshio path
181 from the coast was measured using the latitude of the Kuroshio path at 138.5ºE. Figure 6 shows the time
182 series of the latitude of the Kuroshio path at 138.5ºE. High (low) latitude indicates that the Kuroshio takes
183 a nearshore (offshore) path. From this latitude of the Kuroshio path, we defined the two typical paths of
184 the Kuroshio as follows: the nearshore path is located north of 33ºN (hereafter NP; shaded yellow in Fig.
185 6) and the offshore path is located south of 32.5ºN (hereafter OP; shaded light green in Fig. 6). The results
186 presented in this paper were not sensitive to small changes in these choices (not shown). The numbers of
187 days during which NP and OP occur are 875 (48%) and 389 (21 %) respectively, out of the total 1826
188 days from April 15, 2006 to April 14, 2011, respectively.

189 Using these definitions, we made composites of 8- to 36-day fluctuations for the two typical paths by
190 averaging the daily data belonging to NP and OP. Figure 7a shows the composite map the during NP.
191 Figure 7b, on the other hand, shows the composite map during of OP. The contours in the figures are
192 composites of the 90-day low-pass-filtered SSH. Therefore, the contours show where the background
193 Kuroshio flows, and the thick solid line (0.1-m isoline) represents the Kuroshio path. As intended by our
194 definition, the contours in Figs. 7a and 7b show the nearshore path and the offshore path, respectively.
195 Color shadings in Figs. 7a and 7b indicate the variances of the 8- to 36-day fluctuations during NP and
196 OP, respectively. These figures indicate that the area of high variance of the 8- to 36-day fluctuations is

197 located along the Kuroshio path, and it moves with the Kuroshio path. The peak variance during NP is
198 higher than that during OP.

199 The variance of the 8- to 36-day fluctuations in the Enshu-nada Sea (around 137.5ºE, 34ºN) in Fig. 7b
200 during OP is not low compared with the variance during NP in Fig. 7a, although the region is far from the
201 Kuroshio path during OP as indicated by the thick black line in Fig. 7b. The variance of the 8- to 36-day
202 fluctuations in the Enshu-nada Sea during the OP is also due to the effect of the S-shaped meander,
203 which is indicated by the arrow in Fig. 7b. This is discussed in the next section.

204

205 **4. Typical structures**

206 First, we discuss typical structures during NP. Figure 8 shows a typical time sequence of the
207 development of the 8- to 36-day fluctuations when the Kuroshio Current took a nearshore path. The
208 color shadings in Figs. 8a, 8c, 8e, and 8g are wavelet variances of SSH every 5 days starting on
209 December 27, 2006. The high variances are detected by the wavelet method around the mean positions
210 of the Kuroshio path (thick dashed lines), which are indicated by the 90-day low-pass-filtered SSH
211 isoline of 0.1 m. The relatively low variance near Cape Shionomisaki increases downstream around the
212 Izu Ridge. The variance also increases with time, as shown in Figs. 8a to 8g.

213 The color shadings in Figs. 8b, 8d, 8f, and 8h are wavelet signals of SSH corresponding to the
214 variances in Figs. 8a, 8c, 8e, and 8g. An undulating pattern emerges in these signals. The signals of SSH

along the slowly-varying Kuroshio path (dashed line in Fig 8) are also plotted in Fig. 9. The value was obtained by averaging the signals from 20 km inshore to 20 km offshore along the cross-path axis (Appendix B). Changing 20 km into 40 km or 0 km, for example, does not change the qualitative results in Fig. 9. In Figs. 8 and 9a, a typical low SSH signal and a high SSH signal are tracked by the blue and red arrows, respectively.

Each signal in Figs. 8 and 9a propagates downstream (eastward) with intensified value. Corresponding to the signals, the snapshots of the Kuroshio path (thick solid line in Fig. 8), indicated by the unfiltered SSH isoline of 0.1 m on each day, reveal an undulating pattern relative to the mean Kuroshio path (thick dashed line in Fig. 8). The path of the Kuroshio becomes more undulating, as shown in Figs. 8b to 8h, corresponding to the increase in variance with time (Figs. 8a to 8g). Figure 9 clearly shows that the signals grow downstream of Cape Shionomisaki.

Although a relatively high variance is detected at 135ºE, 32.5ºN, the smooth connection toward the downstream region is hampered by the presence of Cape Shionomisaki when the Kuroshio path (thick black solid line) is located close to Cape Shionomisaki. The gap is indicated by the low variance near Cape Shionomisaki in Figs. 8a to 8c. Propagation of the signals from the upstream region is weak, as shown in Fig. 8b and 8d, and the first half of Fig. 9a. As the Kuroshio path shifts farther offshore from Cape Shionomisaki, the connection from the upstream to the downstream regions becomes smoother. The variance near Cape Shionomisaki is higher (Figs. 8e and 8g) than before. The propagation of a positive

233 (red) signal of SSH passes Cape Shionomisaki in Fig. 8f and 8h, and the second half in Fig. 9a.

234 Figure 10 shows the velocities and temperatures during the same period and for the same dates as in
235 Fig. 8. During this period, the 90-day low-pass-filtered absolute velocity (the shading in the left panels
236 of Fig. 10) was strong in the downstream side of Cape Shionomisaki. Corresponding to the strong
237 velocity, the meridional temperature gradient was sharp on the inshore side of the area with the strong
238 velocity (not shown). Miyama and Miyazawa (2013) described the structure of the strong velocity
239 downstream of Cape Shionomisaki and the accompanying sharp meridional temperature gradient on the
240 inshore side of the velocity. They argued that the strong velocity is a manifestation of the Kuroshio
241 acceleration at Cape Shionomisaki, which often occurs when the Kuroshio takes the nearshore path. The
242 relationship between the Kuroshio acceleration and the 8- to 36-day fluctuations is discussed in Section
243 6.

244 Velocity signals (the vectors in the right panels of Fig. 10) are consistent with the SSH signals in Fig.
245 8: anticyclonic (cyclonic) circulations around high (low) SSHs. Temperature signals (color shadings in
246 the right panels of Fig. 10) also displayed a corresponding undulating pattern. The signals were strong
247 on the inshore side of the Kuroshio path where the background temperature gradient was sharp. While
248 the variance of the 8- to 36-day fluctuations increase with time (color shadings in Fig. 8a, 8c, 8e, and 8g),
249 the background velocity decreased (color shadings in Figs. 10a, 10c, 10e, and 10g).

250 Next, we discuss typical structures during OP. Figures 11 and 12 show a typical time sequence of the

development of the 8- to 36-day fluctuations when the Kuroshio Current takes an offshore path (every 5 days starting on April 25, 2007). Signals of SSH along the Kuroshio path are plotted in Fig. 9b. During this period, the variance (color shadings in the left panels of Fig. 11), signals of the SSH (color shadings in the right panels of Fig. 11), and signals of velocities and temperatures (vectors and color shadings in the right panels of Fig. 13) appeared around the offshore path of the Kuroshio (thick dashed line). Although the patterns appear to be similar to those during the nearshore path, the amplitudes in Figs. 11, 12 and 9b are small compared with those in Figs. 8, 10 and 9a during the nearshore path period. Note that the contour levels in Figs. 8 and 11, Figs. 10 and 12, and Figs. 9a and 9b are different. The background velocity (color shadings in the left panels of Fig. 12) does not show the strong Kuroshio acceleration that is apparent in Fig 10a. The gradient of the values between the upstream and downstream of Cape Shionomisaki along the Kuroshio path appears to be smaller (Fig. 9b) than that during the nearshore path (Fig. 9a) described above.

A unique feature during the offshore period in Figs. 11 and 12 is that there were westward-propagating signals around 34ºN toward the Enshu-nada Sea. A typical high SSH and a corresponding high SST are tracked by the green arrows in Figs. 11 and 12, respectively. These westward signals happened because a westward-flowing branch of the Kuroshio intruded into the Enshu-nada Sea when the S-shaped meander of the Kuroshio around the Izu Ridge was enhanced (the thick solid lines in Figs. 11 and 12). To show how far the Kuroshio path intrudes into the S-shaped meander, a non-filtered

-0.25-m isoline of SSH (red curve) is added to Figs. 11 and 12. Observations of the intrusion of water from the Kuroshio by the westward branch into the coastal areas of the Kumano-nada Sea and the Enshu-nada Sea with a dominant period of about 20 days have been reported (Kimura and Sugimoto 2000). It should be noted that the emergence of the S-shaped meander itself was not the result of the 8- to 36-day fluctuations. The enhanced S-shape (black solid contour relative to black dashed line) continued throughout Fig. 11, indicating that the emergence of the S-shaped meander was caused by lower frequency fluctuations than the 8- to 36-day fluctuations. The emergence of the S-shaped meander is the result of 40- to 80-day fluctuations (not shown), as observed by Kasai et al. (1993) and Takahashi et al. (2011).

Finally, we statistically confirm the typical undulating pattern described above. Fig. 13a shows the horizontal distribution of the correlation (contour) and the regression (color shadings; m/m) of the SSH signal (m) at each point to the SSH signal (m) at point A (139.2ºE, 33.5ºN), which is close to the maximum variance shown in Fig. 7a, using the daily data during NP. As shown in the typical pattern described in the preceding subsection, undulating patterns of plus and minus values appear along the Kuroshio path (thick black solid line). The correlation toward the upstream of Cape Shionomisaki quickly decays. The distance between points A (139.2ºE, 33.5ºN) and A' (136ºE, 33.2ºN) in Fig. 13a corresponds to a wavelength about 300 km (299 km). The lag correlation between the signals of points A and A' becomes maximum (0.35) when A' leads A by 21 days. Therefore, this statistical estimate shows that the

287 wave period is 21 days, and the downstream phase speed is about 14 km/day (0.16 m/s).

288 Figure 13b shows the horizontal distribution of the correlation (contour) and the regression (color
289 shadings; m/m) of the SSH signal (m) at each point to the SSH signal at point B (139.5ºE, 31.8ºN),
290 which is close to the maximum variance shown in Fig. 7b, using the daily data during OP. This figure also
291 shows the undulating patterns of plus and minus values appearing along the Kuroshio path during OP. The
292 continuation of the undulating pattern toward the upstream of Cape Shionomisaki is somewhat clearer
293 than that during NP, but it is still small. The distance between points B (139.5ºE, 31.8ºN) and B' (136.5ºE,
294 33.05ºN) in Fig. 13b corresponds to a wavelength of 314 km. Although the estimate of the wavelength
295 during OP is slightly longer than that during NP, the significance of this difference is not certain, because
296 the current method is a rough estimate based on a pointwise correlation. The lag correlation between the
297 signals of points B and B' becomes maximum (0.19) when B' leads B by 19 days. Therefore, this
298 statistical estimate shows that the wave period is 19 days and that the downstream phase speed is about 17
299 km/day (0.20 m/s).

300

301 **5. Vertical structure**

302 In order to reveal the vertical structure of the 8- to 36-day fluctuations, the color shadings in Fig. 14
303 show vertical sections of the composites of the variances of the zonal velocity (m^2/s^2) plus the variance
304 of the meridional velocity (m^2/s^2), which is equivalent to the eddy kinetic energy. Variances of the

305 velocity (color shadings) along 137ºE shown in both Fig. 14a during NP and Fig. 14b during OP show
306 that the variance is highest at the surface on the inshore (northward) side of the background velocity
307 maximum (90-day low-pass-filtered; contours; m/s). The high variance coincides with the place where
308 the velocity gradient is steep. Slight enhancements of the variances on the offshore (southward) side of the
309 velocity maximum are also found. They coincide with the place of another sharp velocity gradient.
310 Following the background velocities, the variances decay and tilt southward with depth. Because the
311 background velocity is higher during NP than during OP, the variance is higher during NP than during OP.
312 While the features of the variance along 137ºE continue downstream along 138ºE (Figs. 14c and 14d),
313 the variances along 138ºE are more enhanced, and the local maxima of the offshore (southward) side of
314 the background velocity maximum are less clear than along 137ºE.
315 We also show that the composites in the Kuroshio-path coordinate system in Figs. 14e and 14f
316 corresponding the Figs. 14c and 14d, respectively. The results in the Kuroshio-path coordinate system is
317 presented because the composites in the fixed geographical coordinate system might cause artificial
318 diffusion when the latitude of the flow varies in time (Halkin and Rossby 1985; Howe et al. 2009). The
319 results in the Kuroshio-path coordinate system in 14f shows stronger background velocity (dashed
320 contour) and higher velocity variance (color shading and thin contour; m^2/s^2) than the composites in the
321 geographical coordinate system in Fig. 14d during the OP. However, Figs. 14e and 14f still show that
322 the background velocity and the velocity variance are larger during NP than during OP.

6. Relation to the Kuroshio acceleration

In Section 4.1, we mentioned the Kuroshio acceleration at Cape Shionomisaki is a typical occurrence in the 8- to 36-day fluctuations during the nearshore path. Miyama and Miyazawa (2013) studied the sudden acceleration of the Kuroshio jet that often appears off Cape Shionomisaki when the Kuroshio flows near the cape. The velocity discontinuity is accompanied by cold water outcropping on the inshore side downstream of Cape Shionomisaki. Miyama and Miyazawa (2013) proposed that the dynamics of the Kuroshio acceleration are a manifestation of a hydraulic control at Cape Shionomisaki when the Kuroshio approaches the coast. Kawabe (1990) found that, in order to provide a theoretical explanation of their paths, the nearshore non-large-meander path requires a larger Kuroshio acceleration than the offshore non-large-meander path. Because the 8- to 36-day fluctuations also become active during the nearshore path, we discuss the relationship between the Kuroshio acceleration and the 8- to 36-day fluctuations.

The red solid line in Fig. 15 shows the Kuroshio acceleration at Cape Shionomisaki determined using the same definition used by Miyama and Miyazawa (2013): the zonal velocity difference between 135.4ºE, 33.4ºN and 136.2ºE, 33.4ºN at 10-m depth. However, we used the 90-day low-pass-filtered velocity instead of the daily or the monthly values used in Miyama and Miyazawa (2013) because we are interested in the response of the short-term fluctuations to the low-frequency change in the background

341 flow. Because of the cutoff period of the low-pass filter, the Kuroshio acceleration in Fig. 15 in this
342 paper is smaller than that shown in Fig. 10 in Miyama and Miyazawa (2013).
343 As also reported in Miyama and Miyazawa (2013), the Kuroshio acceleration (red solid line in Fig.
344 15) shows a high correlation (0.80) with the latitude of the Kuroshio at 138.5°E (black line in Fig. 15;
345 the same as the red line in Fig. 6), despite the absence of the Kuroshio large meander in the dataset and
346 the different definition of the Kuroshio path compared with that used by Miyama and Miyazawa (2013).
347 In Miyama and Miyazawa (2013), the latitude of the Kuroshio is defined by the location of maximum
348 velocity between 136°E and 140°E, 30.5–35°E at 10-m depth. The high correlation between the Kuroshio
349 acceleration and the Kuroshio latitude means that the Kuroshio acceleration (red solid line in Fig. 15) is
350 stronger during the nearshore path (shaded yellow) than the offshore path (shaded lightgreen) as Kawabe
351 (1990) has shown. Miyama and Miyazawa (2013) showed that the velocity on the downstream side of
352 Cape Shionomisaki is controlled by the Kuroshio acceleration. In fact, the zonal velocity on the
353 downstream side of Cape Shionomisaki at 136.2, 33.4ºN (red dashed line in Fig. 15) shows a high
354 correlation (0.86) with the Kuroshio acceleration (red solid line in Fig. 15).
355 Figure 16 shows the horizontal map of the lagged correlation coefficient (contour) and the regression
356 (color shading; $m^2/(m/s)$) between the Kuroshio acceleration (solid line in Fig. 16; m/s) and the variance
357 of the 8- to 36-day SSH fluctuation (m^2) when the Kuroshio acceleration leads the variance by 30 days.
358 The lead-time was used so that the highest correlation appears in Fig. 16. The high positive correlation

and regression region collocates with the active region of the 8- to 36-day fluctuations in Fig. 5, and especially with the active region during NP in Fig. 7a. The negative correlation and regression in Fig. 16 appears near 140°E, 32°N. This coincides with the active region of the 8- to 36-day fluctuations during OP (Fig. 7b). This negative relation appears because the Kuroshio acceleration tends to be weak during OP. The negative value of the regression (minimum about -0.012) is weaker than the positive value (maximum about 0.018), which reflects that the 8- to 36-day fluctuations are more active during NP than OP. These results suggest that the Kuroshio acceleration has a correlation with the amplitude of the 8- to 36-day fluctuations.

Because the above results imply that the 8- to 36-day fluctuations are more active when the background velocity is stronger, it can be hypothesized that the fluctuations are the result of instability. To examine the degree of instability, we analyzed the local energetics in the same way as in Miyazawa et al. (2004).

The local energy transfer from mean kinetic energy to eddy kinetic energy is expressed as follows (Wells et al. 2000):

$$K = -[\overline{u'u'}\frac{\partial \overline{u}}{\partial x} + \overline{u'v'}(\frac{\partial \overline{u}}{\partial y} + \frac{\partial \overline{v}}{\partial x}) + \overline{v'v'}\frac{\partial \overline{v}}{\partial y}], \qquad (1)$$

where u (v) denotes the eastward (northward) perturbed velocity, and x (y) denotes the zonal (meridional) direction. The prime and overbar quantities represent fluctuations and time-means, respectively. When K is positive, it can be interpreted that the barotropic instability generates

377 disturbances.

378 Similarly, the energy transfer from mean potential energy to eddy kinetic energy is judged by the

379 following term:

380 $$P = -g\frac{\overline{u'\rho'}(\partial\overline{\rho}/\partial x)+\overline{v'\rho'}(\partial\overline{\rho}/\partial y)}{\rho_0 d\rho_b(z)/dz}, \quad (2)$$

381 where g is the gravity acceleration; ρ, ρ_0, and $\rho_b(z)$ are density, reference density, and background

382 density, respectively; and z denotes vertical direction. When P is positive, it can be interpreted that the

383 baroclinic instability generates disturbances. A part of P is transformed into eddy kinetic energy through

384 the buoyancy term, $B = -g\overline{\rho' w'}$, where w is the perturbed vertical velocity. However, the

385 complicated distribution of vertical velocity owing to rough bottom topography prevents us from

386 obtaining a meaningful view from the plot of B (Wells et al. 2000; Miyazawa et al. 2004).

387 Here, the wavelet 8- to 36-day band-pass filtered signals are used for the prime quantities. The

388 wavelet 90-day low-pass-filter is used to obtain the overbar quantities.

389 Figure 17a shows the vertical section of composites of the energy conversion term K during NP along

390 the across-path coordinate at 137ºE. High K values (color shadings) appear where the horizontal velocity

391 gradient is sharp on both sides of the velocity (contour) maximum at the surface, and is especially high

392 on the inshore (northward) side of the velocity maximum. Figure 17b shows the vertical section of

393 composites of the energy conversion term P (color shadings) during NP along the across-path coordinate

394 along 137ºE. A high *P* appears where the horizontal temperature (contour) gradient is sharp on the inshore
395 (northward) side of the velocity maximum at the subsurface. The location is where the vertical gradient of
396 the velocity in Fig. 17a is strong from the thermal wind relationship. These high *K* and *P* values indicate
397 that both barotropic and baroclinic instabilities are favorable for generating disturbances. This is
398 consistent with the existence of the high variance of the velocity on the inshore (northward) side of the
399 velocity maximum in Fig. 14a.

400 Figures 17c and 17d show that high *K* and *P* values (color shadings) also appear in the composites
401 during OP. There are still high values on the inshore side of the velocity maximum. However, the *K* and
402 *P* values are much smaller than those during NP (Figs. 17a and 17b). This reflects a weaker velocity and
403 accompanying temperature gradient during OP (contours in Fig. 17c and 17d) than during NP (contours
404 in Figs. 17a and 17b).

405 Figure 18a shows the barotropic conversion term *K* during NP in the geographical horizontal map at
406 the surface (10-m depth), which is the depth where the value of *K* is highest (Fig. 17a). Figure 18b
407 shows the baroclinic conversion term *P* during NP at 100-m depth, which is the depth where the value of
408 *P* is highest (Fig. 17b). The *K* and *P* values are high around the Kuroshio path (thick black solid line),
409 especially on the inshore side of the path. The high values stretch downstream from Cape Shionomisaki.
410 This is because the Kuroshio acceleration at Cape Shionomisaki generates a strong velocity gradient and
411 temperature gradient, especially on the inshore side of the Kuroshio Current (Miyama and Miyazawa

412 2013). The high positive energy conversion rates on the downstream side of Cape Shionomisaki explain
413 why the 8- to 36-day fluctuations are enhanced from near Cape Shionomisaki toward the downstream
414 region around the Izu Ridge.

415 Figures 18c and 18d during OP correspond to Figs. 18a and 18b during NP. The energy conversion
416 terms in Figs. 18c and 18d are small compared with those in Figs. 18a and 18b because the Kuroshio
417 acceleration is small during OP. However, the values of *K* and *P* downstream of Cape Shionomisaki all
418 along the Kuroshio path are still relatively higher than those of the surrounding regions. This explains
419 the downstream enhancement of the 8- to 36-day fluctuations during OP, albeit weaker than NP.

420 The relationship of the Kuroshio acceleration with the energy conversion terms can also be confirmed
421 in the time series of *K* and *P* integrated over 136–139ºE, 31–35ºN from 0 to 1000-m depth (Fig. 19).
422 The Kuroshio acceleration (m/s; black line in Fig. 19, same as the red line in Fig. 15) shows positive
423 correlations with the integrated *K* value (m^5/s^3; red line in Fig. 19), highest coefficient (0.50) when the
424 acceleration leads by 2 days, and with the integrated *P* (m^5/s^3; blue line in Fig. 19), highest coefficient
425 (0.61) when the acceleration leads by 23 days, respectively. The reason for the different lead-times for *K*
426 and *P* is unknown, and will be a subject of a future study. The integrated *K* value is overall larger than
427 the integrated *P* value, suggesting the relative importance of the barotropic instability. The ratio of *K* to
428 *P* does not show any significant correlation to the Kuroshio acceleration (not shown). Therefore, the
429 Kuroshio acceleration does not seem to affect the ratio of *K* to *P*.

Figure 18 also shows that the energy conversion terms are negative on the upstream side of Cape Shionomisaki, indicating that the eddy energy is absorbed into the mean energy. This explains why the variances near Cape Shionomisaki decrease in Fig. 5.

7. Summary and Discussion

This study describes 8- to 36-day fluctuations south of Japan using the JCOPE2 reanalysis data with a horizontal resolution of 1/36º. To detect the short-term fluctuations, we applied wavelet analysis. The amplitude of the 8-to 36-day fluctuations increases eastward from Cape Shionomisaki toward downstream around the Izu Ridge. The fluctuations of the 8- to 36-day period band are more active during the period of the nearshore non-large-meander path of the Kuroshio than during the period of the offshore non-large-meander path. The fluctuations of the 8- to 36-day period band appear as frontal waves on the Kuroshio Current. The waves have a wavelength of about 300 km, and the signals propagate eastward.

We found a relationship between the Kuroshio acceleration at Cape Shionomisaki and the amplitude of the 8- to 36-day period band. An analysis of energy conversion terms shows that both barotropic and baroclinic instabilities are important for generating eddies corresponding to the 8- to 36-day fluctuations. If the Kuroshio acceleration is a super critical flow resulting from hydraulic control, as proposed by Miyama and Miyazawa (2013), generation of a disturbance can be interpreted as a kind of hydraulic

448 jump. A hydraulic jump is an abrupt transition process, which is often accompanied by turbulence and
449 undulating patterns, from an unstable supercritical flow to a subcritical flow (Pratt and Whitehead 2007).
450 Because the Kuroshio acceleration produces a strong velocity shear and a sharp temperature gradient
451 on the inshore side of the velocity maximum, the variance of the velocity is strong on the inshore side of
452 the velocity maximum. As the velocity core shifts southward with depth, the high variance of the
453 velocity moves southward with depth. The variance of the SSH, which reflects the underlying physics is
454 high around the Kuroshio path. Because the Kuroshio acceleration is strong during the nearshore path,
455 the variance of the 8- to 36-day fluctuations is higher during the nearshore path than during the offshore
456 path.
457 The signals upstream of Cape Shionomisaki do not show a high correlation with the signals
458 downstream. From the local minimum around Cape Shionomisaki, the variance is enhanced toward the
459 downstream region around the Izu Ridge. The reason for the small upstream influence is partly because
460 the condition at Cape Shionomisaki is adverse to eddy growth (negative values of the conversion terms
461 in Fig. 18), and partly because the local growth of disturbances downstream diminishes the upstream
462 influences. Because these factors are relatively small along the path during the offshore path, the
463 correlation between upstream and downstream are slightly higher than during the nearshore path. In the
464 Gulf Stream, Savidge (2004) found that high-frequency (3- to 8-day) fluctuations decay almost
465 completely downstream of Cape Hatteras, with growth in the longer-period (30- to 120-day) fluctuations.

466 Comparing similarities and differences between the Kuroshio and the Gulf Stream is an interesting topic.
467 Because of the local enhancement of the disturbance, we focused on the region between Cape
468 Shionomisaki and the Izu Ridge in this study and did not discuss fluctuations upstream of Cape
469 Shionomisaki. A small upstream influence in the variance does not exclude the possibility that signals
470 from upstream sometimes flow downstream of Cape Shionomisaki and/or that small activities upstream
471 can be a trigger of instability on the downstream side. The influence of the fluctuations upstream of
472 Cape Shionomisaki will be further investigated in a future study.
473 Another interesting subject for a future study would be to determine how the short-term fluctuations
474 in this study affect fluctuations further downstream. Just as the Kuroshio path affects the fluctuations in
475 this study, Sugimoto and Hanawa (2011) showed that the Kuroshio path also affects short-term
476 fluctuations in the Kuroshio Extension. Unfortunately, we cannot discuss the relationship between the
477 short-term fluctuations in this study and eddy activities downstream because the data used in this study
478 do not extend past the eastern boundary at 142ºE.
479 While some studies have combined the fluctuations of periods of around 10 days and 20–30 days
480 (Itoh and Sugimoto 2008), other studies treated them separately (Kimura and Sugimoto 1993; Hinata et
481 al. 2008; Ramp et al. 2008). When the 8-to 36-day fluctuations are separated into 8- to 16-day and 16- to
482 36-day fluctuations, the horizontal distributions of the variance of both frequency bands show nearshore
483 peaks similar to Fig. 5 (not shown). The time series of the variance of both the 8- to 16-day and 16- to

484 36-day period bands averaged over 137−140°E, 33−34°N around the peak region in Fig.5 show similar
485 timings of peaks (Fig. 20) although they are not exactly the same. The correlation between the two
486 curves in Fig. 20 is 0.58 (the correlation becomes maximum at 0-day lag). Figure 20 also shows that the
487 variance of the 8- to 16-day fluctuations (black curve) is overall much smaller than that of the 16- to
488 36-day fluctuations (red curve). Excluding the 8-to 16-day fluctuations from 8- to 36-day fluctuations
489 does not affect the conclusions presented in this paper (not shown). Therefore, there was no particular
490 reason to treat 8- to 16-day fluctuations separately in this study. It should be noted, however, that the
491 fluctuations with periods of around 10 days might be only minimally resolved by data of one-day
492 intervals. Therefore, we cannot deny the possibility that the variance of the 8- to 16-day fluctuations is
493 underestimated. We might revisit this issue on these frequencies in a future study using a different
494 dataset and/or methodology.
495 An interesting question is why disturbances of periods of around 8- to 36-days are generated. Frontal
496 waves of similar frequencies have been reported in other coastal areas in Japan: in the East China Sea
497 (Sugimoto et al. 1988; Qiu et al. 1990; James et al. 1999), in the Tokara Strait (Qiu et al. 1990; Maeda et
498 al. 1993; Feng et al. 2000), south of Shikoku (Awaji et al. 1991), near the separation point of the
499 Kuroshio to the Kuroshio Extension (Itoh and Sugimoto 2008), and in the Kuroshio Extension (Tracey
500 et al. 2012). Frontal wave disturbances have been also found in the Gulf Stream (Lee and Atkinson
501 1983; Tracey and Watts 1986; Oey 1988; Savidge 2004). Itoh and Sugimoto (2008) successfully applied

502 the analytical model of baroclinic instability by Pedlosky (1987) to the variability of the Kuroshio near
503 the separation point from the western boundary, and they also discussed similar fluctuations in other
504 regions of the Kuroshio. However, to explain the variability in this paper, the theory of pure baroclinic
505 instability is insufficient because the analysis of the energy conversion terms shows that barotropic
506 instability is also important. Using an instability analysis and a theoretical model, we will seek factors to
507 determine the time and spatial scale of frontal waves in future studies.

508 Discussion of the 40- to 80-day fluctuations will be addressed in another paper. In contrast to the 8- to
509 36-day fluctuations, the peak variance of the 40- to 80-day fluctuations during OP is higher than that
510 during NP (Appendix A). Because the peak region of 40- to 80-day fluctuations overlaps with the peak
511 region of 8- to 36-day fluctuations on the downstream side of the Izu-ridge, the interaction between them
512 might be important here. A full understanding of the short-term fluctuations on the downstream side of
513 the Izu-ridge is beyond the scope of this study and needs further investigation.

514 We identified the properties of short-term fluctuations in the form of frontal waves and determined
515 their relationship with the background velocity and the Kuroshio path. This knowledge will be beneficial
516 for predicting when short-term fluctuations become active. As mentioned in the Introduction, the frontal
517 waves of the Kuroshio Current affect biological activities and fisheries. Therefore, a better
518 understanding of these short-term fluctuations will be important for the management of ecological
519 environments.

520

Appendix A. 40- to 80-day fluctuation

We briefly describe the distribution of the 40- to 80-day fluctuations. Figures 21a and 21b show a composite map of the 40- to 80-day fluctuations during NP and OP, respectively. In contrast to the 8- to 36-day fluctuations in Fig 7, the peak variance of the 40- to 80-day fluctuations during OP (Fig. 21b) is higher than that during NP (Fig. 21a). The higher variance around the Izu ridge during OP than NP is consistent with the observations of Kasai et al. (1993) and Takahashi et al. (2011).

Also in the Enshu-nada Sea (around 33.5ºN, 138ºE), the variance of the 40- to 80-day fluctuations during OP is higher than that during NP. This is consistent with the past observation by Kasai et al. (1993), in that the westward intrusion of Kuroshio water into the Enshu-nada Sea often occurred with a 50-day period caused by the S-shaped meander of the Kuroshio path near the Izu Ridge. A vestige of the S-shaped meander can be seen in the time-averaged SSH during the OP in Fig. 21b (pointed at by the black arrow).

Appendix B. Kuroshio-path coordinate system

In some of the analyses in this paper, a Kuroshio-path coordinate system was used. This is because averages of variances and signals could become diffused in the fixed geophysical coordinate system (Halkin and Rossby 1985; Howe et al. 2009) as the latitude and direction of the Kuroshio change with time. An example of the Kuroshio-path coordinate system at 138ºE is schematically shown in Fig. 22.

539 The Kuroshio path coordinate at 138ºE means an origin is defined on the Kuroshio path at 138ºE. The
540 along-path axis is oriented to the downstream tangential direction of the curve of the Kuroshio path. The
541 cross-path axis is perpendicular to the along-path axis, and its direction is positive to the left of the
542 along-path axis. In this paper, “inshore” and “offshore” directions are used interchangeably to mean
543 “positive” and “negative” in the cross-pass direction, respectively. The latitude of the origin varies with
544 time as the Kuroshio path moves. Although we could define the stream-coordinate using the velocity
545 direction like Halkin and Rossby (1985) and Howe et al. (2009), we used the curve of the Kuroshio path
546 defined by the SSH isoline of 0.1 m for consistency with the other parts of this paper. The directions of
547 the along-path and the maximum velocity at the surface agree well. Therefore, the velocity maximum at
548 the surface in the Kuroshio-path coordinate is around the origin (zero on the cross-path axis; Figs 14 e
549 and 14f and Figs. 17a and 17c.). Because we are interested in the response of the short-term fluctuations
550 to the low-frequency change of the background flow, we used the 90-day low-pass-filtered SSH rather
551 than the instantaneous one. A similar method to investigate the variability along a slowly varying path
552 was used by Tracey et al. (2012) in a study of the frontal waves in the Kuroshio Extension.
553

Acknowledgment

This work is a part of the Japan Coastal Ocean Predictability Experiment (JCOPE) promoted by the Japan Agency for Marine-Earth Science and Technology (JAMSTEC). Tomohiko Tsunoda conducted the calculation of the JCOPE2 with 1/36 resolution. We would like to thank Sergey M. Varlamov, Takuji Waseda, Humio Mitsudera, and Sourav Sil for their helpful discussions. The authors would like to thank Enago (www.enago.jp) and Textcheck (www. textcheck.com) for the English language review. The authors would like to thank the editor of this paper, Leo Oey, and two anonymous reviewers for their suggestions, which helped to improve the manuscript.

562 **References**

563 Awaji T, Akitomo K, Imasato N (1991) Numerical Study of Shelf Water Motion Driven by the

564 Kuroshio: Barotropic Model. J Phys Oceanogr 21 (1):11-27.

565 doi:10.1175/1520-0485(1991)021<0011:nsoswm>2.0.co;2

566 Feng M, Mitsudera H, Yoshikawa Y (2000) Structure and Variability of the Kuroshio Current in Tokara

567 Strait. J Phys Oceanogr 30 (9):2257-2276.

568 doi:10.1175/1520-0485(2000)030<2257:savotk>2.0.co;2

569 Guo X, Hukuda H, Miyazawa Y, Yamagata T (2003) A Triply Nested Ocean Model for Simulating the

570 Kuroshio—Roles of Horizontal Resolution on JEBAR. J Phys Oceanogr 33 (1):146-169.

571 doi:10.1175/1520-0485(2003)033<0146:atnomf>2.0.co;2

572 Halkin, D., and T. Rossby, 1985: The Structure and Transport of the Gulf Stream at 73°W. J. Phys.

573 Oceanogr., 15, 1439-1452, doi:10.1175/1520-0485(1985)015<1439:tsatot>2.0.co;2.

574 Hinata H, Yanagi T, Satoh C (2008) Sea level response to wind field fluctuation around the tip of the Izu

575 Peninsula. J Oceanogr 64 (4):605-620. doi:10.1007/s10872-008-0051-z

576 Howe, P. J., K. A. Donohue, and D. R. Watts, 2009: Stream-coordinate structure and variability of the

577 Kuroshio Extension. Deep-Sea Res. I, 56, 1093-1116, doi:10.1016/j.dsr.2009.03.007.

578 Itoh S, Sugimoto T (2008) Current variability of the Kuroshio near the separation point from the western

579 boundary. J Geophys Res 113 (C11):C11020-C11020. doi:10.1029/2007jc004682

James C, Wimbush M, Ichikawa H (1999) Kuroshio Meanders in the East China Sea. J Phys Oceanogr 29 (2):259-272. doi:10.1175/1520-0485(1999)029<0259:kmitec>2.0.co;2

Kalnay E, Kanamitsu M, Kistler R, Collins W, Deaven D, Gandin L, Iredell M, Saha S, White G, Woollen J, Zhu Y, Chelliah M, Ebisuzaki W, Higgins W, Janowiak J, Mo KC, Ropelewski C, Wang J, Leetmaa A, Reynolds R, Jenne R, Joseph D (1996) The NCEP/NCAR 40-year reanalysis project. Bull Amer Meteorol Soc 77 (3):437-471. doi:10.1175/1520-0477(1996)077<0437:TNYRP>2.0.CO;2

Kasai A, Kimura S, Nakata H, Okazaki Y (2002) Entrainment of coastal water into a frontal eddy of the Kuroshio and its biological significance. J Mar Syst 37 (1-3):185-198. doi:10.1016/S0924-7963(02)00201-4

Kasai A, Kimura S, Sugimoto T (1993) Warm water intrusion from the Kuroshio into the coastal areas south of Japan. J Oceanogr 49 (6):607-624. doi:10.1007/BF02276747

Kawabe M (1985) Sea level variations at the Izu Islands and typical stable paths of the Kuroshio. J Oceanogr 41 (5):307-326. doi:10.1007/bf02109238

Kawabe M (1987) Spectral properties of sea level and time scales of Kuroshio path variations. J Oceanogr Soc Japan 43 (2):111-123. doi:10.1007/bf02111887

Kawabe M (1990) A steady model of typical non-large-meander paths of the Kuroshio Current. J Oceanogr Soc Japan 46 (2):55-67. doi:10.1007/bf02124815

598 Kimura S, Choo HS, Sugimoto T (1994) Characteristics of the eddy caused by Izu-Oshima Island and
599 the Kuroshio branch current in Sagami Bay, Japan. J Oceanogr 50 (4):373-389.
600 doi:10.1007/BF02234961
601 Kimura S, Kasai A, Nakata H, Sugimoto T, Simpson JH, Cheok JVS (1997) Biological productivity of
602 meso-scale eddies caused by frontal disturbances in the Kuroshio. ICES J Mar Sci 54
603 (2):179-192. doi:10.1006/jmsc.1996.0209
604 Kimura S, Sugimoto T (1987) Short period fluctuations in oceanographic and fishing conditions in the
605 coastal area of Kumano-nada Sea. Nippon Suisan Gakkaishi 53 (4):585-593
606 http://agriknowledge.affrc.go.jp/RN/2010350534.pdf
607 Kimura S, Sugimoto T (1993) Short-period fluctuations in meander of the Kuroshio path off Cape
608 Shiono-misaki. J Geophys Res 98 (C2):2407-2418. doi:10.1029/92JC02582
609 Kimura S, Sugimoto T (2000) Two processes by which short-period fluctuations in the meander of the
610 Kuroshio affect its countercurrent. Deep-Sea Res I 47 (4):745-754.
611 doi:10.1016/s0967-0637(99)00067-9
612 Lee TN, Atkinson LP (1983) Low-frequency current and temperature variability from Gulf Stream
613 frontal eddies and atmospheric forcing along the southeast U.S. outer continental shelf. J
614 Geophys Res 88 (C8):4541-4541. doi:10.1029/JC088iC08p04541
615 Maeda A, Yamashiro T, Sakurai M (1993) Fluctuation in volume transport distribution accompanied by

616 the Kuroshio front migration in the Tokara Strait. J Oceanogr 49 (2):231-245.
617 doi:10.1007/bf02237290
618 Mitsudera H, Taguchi B, Waseda T, Yoshikawa Y (2006) Blocking of the Kuroshio large meander by
619 baroclinic interaction with the Izu Ridge. J Phys Oceanogr 36 (11):2042-2059.
620 doi:10.1175/JPO2945.1
621 Miyama T, Miyazawa Y (2013) Structure and dynamics of the sudden acceleration of Kuroshio off Cape
622 Shionomisaki. Ocean Dyn 63 (2-3):265-281. doi:10.1007/s10236-013-0591-7
623 Miyazawa Y, Guo X, Yamagata T (2004) Roles of Mesoscale Eddies in the Kuroshio Paths. J Phys
624 Oceanogr 34 (10):2203-2222. doi:10.1175/1520-0485(2004)034<2203:romeit>2.0.co;2
625 Miyazawa Y, Kagimoto T, Guo X, Sakuma H (2008) The Kuroshio large meander formation in 2004
626 analyzed by an eddy-resolving ocean forecast system. J Geophys Res 113 (C10):C10015-C10015.
627 doi:10.1029/2007jc004226
628 Miyazawa Y, Zhang R, Guo X, Tamura H, Ambe D, Lee J-S, Okuno A, Yoshinari H, Setou T, Komatsu
629 K (2009) Water mass variability in the western North Pacific detected in a 15-year eddy
630 resolving ocean reanalysis. J Oceanogr 65 (6):737-756. doi:10.1007/s10872-009-0063-3
631 Oey L-Y (1988) A Model of Gulf Stream Frontal Instabilities, Meanders and Eddies along the
632 Continental Slope. J Phys Oceanogr 18 (2):211-229.
633 doi:10.1175/1520-0485(1988)018<0211:amogsf>2.0.co;2

634 Oey L-Y, Chen P (1992) A Nested-Grid Ocean Model: With Application to the Simulation of Meanders
635 and Eddies in the Norwegian Coastal Current. J Geophys Res 97 (C12):20063-20086.
636 doi:10.1029/92jc01991
637 Okazaki Y, Nakata H, Kimura S, Kasai A (2003) Offshore entrainment of anchovy larvae and its
638 implication for their survival in a frontal region of the Kuroshio. Mar Ecol Prog Ser 248:237-244.
639 doi:10.3354/meps248237
640 Pedlosky J (1987) Geophysical Fluid Dynamics, 2nd Ed. Springer-Verlag, New York
641 Pratt LJ, Whitehead JA (2007) Rotating hydraulics: nonlinear topographic effects in the ocean and
642 atmosphere. Springer, New York
643 Qiu B, Chen S (2005) Variability of the Kuroshio Extension Jet, Recirculation Gyre, and Mesoscale
644 Eddies on Decadal Time Scales. J Phys Oceanogr 35 (11):2090-2103. doi:10.1175/jpo2807.1
645 Qiu B, Toda T, Imasato N (1990) On Kuroshio front fluctuations in the East China Sea using satellite
646 and in situ observational data. J Geophys Res 95 (C10):18191-18191.
647 doi:10.1029/JC095iC10p18191
648 Ramp SR, Barrick DE, Ito T, Cook MS (2008) Variability of the Kuroshio Current south of Sagami Bay
649 as observed using long-range coastal HF radars. J Geophys Res 113 (C6):C06024-C06024.
650 doi:10.1029/2007jc004132
651 Saito K, Ishida J-i, Aranami K, Hara T, Segawa T, Narita M, Honda Y (2007) Nonhydrostatic

652 Atmospheric Models and Operational Development at JMA. J Meteorol Soc Jpn 85B:271-304.
653 doi:10.2151/jmsj.85B.271
654 Savidge DK (2004) Gulf Stream Meander Propagation Past Cape Hatteras. J Phys Oceanogr 34
655 (9):2073-2085. doi:10.1175/1520-0485(2004)034<2073:gsmppc>2.0.co;2
656 Sugimoto S, Hanawa K (2011) Relationship between the path of the Kuroshio in the south of Japan and
657 the path of the Kuroshio Extension in the east. J Oceanogr 68 (1):219-225.
658 doi:10.1007/s10872-011-0089-1
659 Sugimoto T, Kimura S, Miyaji K (1988) Meander of the Kuroshio front and current variability in the
660 East China Sea. J Oceanogr Soc Japan 44 (3):125-135. doi:10.1007/bf02302619
661 Taft AB (1978) Structure of the Kuroshio south of Japan. J Mar Res 16:77-117
662 Taira K, Teramoto T (1981) Velocity fluctuations of the Kuroshio near the Izu Ridge and their
663 relationship to current path. Deep-Sea Res A 28 (10):1187-1197.
664 doi:10.1016/0198-0149(81)90055-8
665 Takahashi D, Morimoto A, Nakamura T, Hosaka T, Mino Y, Dang VH, Saino T (2012) Short-term flow
666 and water temperature fluctuations in Sagami Bay, Japan, associated with variations of the
667 Kuroshio during the non-large-meander path. Prog in Oceanogr 105:47-60.
668 doi:10.1016/j.pocean.2012.04.012
669 Takahashi D, Morimoto A, Nakamura T, Hosaka T, Mino Y, Saino T (2011) Flow variability with

periods of 50-70 days in Sagami Bay, Japan during the offshore non-large-meander path of the Kuroshio (in Japanese with English abstract and legends). Oceanogr in Jpn 20 (3,4):59-83

Torrence C, Compo GP (1998) A Practical Guide to Wavelet Analysis. Bull Amer Meteorol Soc 79 (1):61-78. doi:10.1175/1520-0477(1998)079<0061:apgtwa>2.0.co;2

Tracey KL, Watts DR (1986) On Gulf Stream meander characteristics near Cape Hatteras. J Geophys Res 91 (C6):7587-7587. doi:10.1029/JC091iC06p07587

Tracey, K. L., D. R. Watts, K. A. Donohue, and H. Ichikawa, 2012: Propagation of Kuroshio Extension Meanders between 143° and 149°E. J. Phys. Oceanogr., 42, 581-601, doi:10.1175/jpo-d-11-0138.1.

Waseda T, Mitsudera H (2002) Chaotic Advection of the Shallow Kuroshio Coastal Waters. J Oceanogr 58 (5):627-638. doi:10.1023/a:1022882004769

Wells NC, Ivchenko VO, Best SE (2000) Instabilities in the Agulhas Retroflection Current system: A comparative model study. J Geophys Res 105 (C2):3233-3241. doi:10.1029/1999jc900283

685 **Figure captions**

686 **Fig. 1** Map off the southern coast of Japan. *Color shading* and *thin contour lines* show bottom
687 topography (m). The nearshore non-large-meander path and the offshore non-large-meander path of the
688 Kuroshio Current are schematically illustrated.

689

690 **Fig. 2 a** Time series of the sea level at 139ºE 33.25ºN. **b** The local wavelet power spectrum of the time
691 series using the Morlet wavelet, normalized by $1/\sigma^2$ ($\sigma^2 = 0.54$ m^2) (*color shadings*). The vertical axis is
692 the wavelet scale (periods in days). The bottom axis is time (year). *Thick contours* enclose regions of
693 greater than 95% confidence for a red-noise process with a lag-1 coefficient of 0.99. *Cross-hatched*
694 regions indicate the "cone of influence", where edge effects become important.

695

696 **Fig. 3** Global wavelet spectrum (*thick black solid line*) obtained from the wavelet spectrum in Fig. 2b,
697 and the 95% confidence level for the global wavelet spectrum (*thin black dashed line*), assuming a lag-1
698 coefficient of 0.99. The vertical axis is the wavelet scale (periods in days). The vertical axis of the global
699 wavelet spectrum is normalized by $1/\sigma^2$ ($\sigma^2 = 0.54$ m^2).

700

701 **Fig. 4** Time series of the wavelet "variance" (*red line*; m^2; axis on the left) and "signal" (*black line*; m;
702 axis on the right) calculated from the time series in Fig. 2a for the 8- to 36-day period band.

703

704 **Fig. 5** Horizontal distributions of the wavelet variance of SSH for the 8- to 36-day period band (*color*
705 *shadings*; m^2) averaged over the whole analysis time period (from April 15, 2006 to April 14, 2011).
706 *Contours* show the unfiltered SSH (m) averaged over the same period. *Green line* shows the 1500-m
707 isodepth contour.

708

709 **Fig. 6** Time series of the latitude of the Kuroshio path at 138.5ºE. The NP and OP periods are shaded
710 *yellow* and *light green*, respectively.

711

712 **Fig. 7** Composite maps of the variance (*color shadings*, m^2) and 90-day low-pass-filtered SSH
713 (*contour*, m) for the 8- to 36-day fluctuations. *Thick contour* is the 0.1-m contour of 90-day
714 low-pass-filtered SSH which represents the Kuroshio path. **a** During NP. **b** During OP. The arrows in **b**
715 points to the contour of the vestige of the S-shaped SSH meander.

716

717 **Fig. 8** A typical time sequence of the development of the 8- to 36-day fluctuations. *Color shading* and
718 *thin contours* in **a** and **b** are the wavelet variance (m^2) and signal (m) of SSH on December 27, 2006,
719 respectively. *Black solid (dashed) line* represents the Kuroshio path shown by the non-filtered (90-day
720 low-pass-filtered) 0.1-m isoline of SSH. **c**, **d** On January 1, 2007. **e, f** On January 6, 2007. **g, h** On January

11, 2007. In **b, d, f,** and **h**, a low and a high SSH signal are tracked by *a blue and a red arrow*, respectively.

Fig. 9 a Along-path–time diagram of the signal of SSH (*color shading and contour*, m) from December, 16, 2006 to January, 21 2007. The signal was averaged from 20 km inshore to 20 km offshore along the cross-path axis. The *horizontal dashed lines* correspond to the dates in Figs. 8b, 8d, 8f, and 8h, respectively. The *vertical dashed line* corresponds to the longitude of Cape Shionomisaki. The low and high SSH tracked by the *arrows* in Fig. 8 are pointed by *a blue and a red arrow*, respectively. **b** Along-path–time diagram for April 16, 2007 to May 21, 2007. The *horizontal dashed lines* correspond to the dates in Figs. 11b, 11d, 11f, and 11h, respectively. The low and high SSH tracked by the *arrows* in Fig. 11 are pointed by *a blue and a red arrow*, respectively. Everything else is the same as in **a**.

Fig. 10 *Color shadings* and *thin contours* in the left panels show the 90-day low-pass-filtered absolute velocities (m/s). *Vectors* and *color shadings* in the right panels are 8- to 36-day wavelet band-pass-filtered velocities (m/s) and temperatures (ºC) at 50-m depth. Everything else is the same as in Fig. 8.

Fig. 11 Same as Fig. 8 except that **a, b** on April 25, 2007; **c, d** on April 30, 2007; **e, f** on May 5, 2007; and **g, h** on May 10, 2007. Additional *red lines* are the non-filtered -0.25-m isoline of SSH. Additional *green arrows* track a westward-moving high SSH.

739

740 **Fig. 12** Same as Fig. 10 except that **a, b** on April 25, 2007; **c, d** on April 30, 2007; **e, f** on May 5,
741 2007; and **g, h** on May 10, 2007. Newly added *red lines* are the non-filtered -0.25-m isoline of SSH.
742 Newly added *green arrows* track a westward-moving high SST.

743

744 **Fig. 13 a** Horizontal distribution of the correlation (*contour*) and the regression (*color shading*; m/m)
745 of the SSH signal of the 8- to 36-day fluctuations to the SSH signal at point A (139.2ºE, 33.5ºN), which
746 is around the maximum variance of Fig. 7a, using only daily data during NP. **b** Same as **a** but to the signal
747 at point B (139.5ºE, 31.8ºN), which is around the maximum in the variance of Fig. 7b, using only daily
748 data during OP. The significant regions with 99 % confidence level are plotted.

749

750 **Fig. 14** *Color shadings* and thin contours show the vertical sections of the composites of the variances
751 of the zonal velocity plus the variance of the meridional velocity (m^2/s^2). *Dashed contours* at 0.6, 1.0
752 and 1.4 m/s show 90-day low-pass-filtered absolute velocities (m/s). Vertical axis is depth (m).
753 Horizontal axis is latitude for **a**, **b**, **c** and **d**. Horizontal axis is the cross-path axis (km) for **e** and **f**. **a**
754 Along 137ºE during NP. **b** Along 137ºE during OP. **c** Along 138ºE during NP. **d** Along 138ºE during OP.
755 **e** and **f** are the composites during NP and OP in the Kuroshio-path coordinate at 138ºE, respectively.

756

757 **Fig. 15** Time series of the zonal velocity increase from 135.4ºE, 33.4ºN to 136.2, 33.4ºN (*red solid*
758 *line;* m/s; axis on the left) and the velocity at 136.2ºE, 33.4ºN (*dashed line*; m/s; axis on the left). The
759 90-day low-pass-filtered zonal velocity at 10-m depth was used. The *black solid line* is the latitude of the
760 Kuroshio path (the same as the *red line* in Fig. 6; axis on the right). The NP and OP periods are shaded
761 *yellow* and *light green*, respectively.
762
763 **Fig. 16** Horizontal map of the correlation coefficient (*contour*) and the regression (*color shading* and
764 *thin contours*; $m^2/m/s$) between the variance of the 8- to 36-day SSH fluctuation (m^2) and the Kuroshio
765 acceleration (*the solid line* in Fig. 17; m/s) using the daily data from April 15, 2006 to April 14, 2011
766 when the Kuroshio acceleration leads the variance by 30 days. The significant regions with 99 %
767 confidence level are plotted.
768
769 **Fig. 17** Vertical sections of composites of the energy conversion terms (*color shadings* and *thin*
770 *contours*; 10^{-6} m^2/s^3) in the Kuroshio-path coordinate at 137ºE. **a** *K* during NP. **b** *P* during NP **c** *K* during
771 OP. **d** *P* during OP. *Dashed contours* at 0.6, 1.0 and 1.4 m/s in **a** and **c** are the background (90-day
772 low-pass-filtered) absolute velocity (m/s) during NP and OP, respectively. *Dashed contours* in **b** and **d**
773 are the background (90-day low-pass-filtered) temperature (ºC) during NP and OP, respectively. The
774 contour interval for the temperatures is 2ºC. Vertical axis is depth (m). Horizontal axis is the cross-path

775 axis (km).

776

777 **Fig. 18** Horizontal maps of composites of the energy conversion terms (*color shadings* and *thin*

778 *contours*; 10^{-6} m^2/s^3). **a** *K* at 10-m depth during NP. **b** *P* at 100-m depth during NP. **c** *K* at 10-m depth

779 during OP. **d** *P* at 100-m depth during OP. *Thick solid lines* are Kuroshio paths (90-day low-pass filtered

780 0.1-m SSH contours).

781

782 **Fig. 19** Time series of the energy conversion terms *K* (*red line*) and *P* (*blue line*) integrated over 136–

783 139ºE, 31–35ºN from 0 to 1000-m depth (10^5 m^5/s^3; axis on the left). *The black line* is the Kuroshio

784 acceleration (m/s; axis on the right, same as the *solid red line* in Fig. 15). The NP and OP periods are

785 shaded *yellow* and *light green*, respectively.

786

787 **Fig. 20** Time series of the variances of the 8- to 16-day period band (*black curve*) and of the 16- to

788 36-day period band (*red curve*) averaged over 137–140ºE, 33–34ºN.

789

790 **Fig. 21** Same as Fig. 7 except for the 40- to 80-day period band.

791

792 **Fig. 22** Schematic diagram of the Kuroshio-path coordinate system at 138ºE.

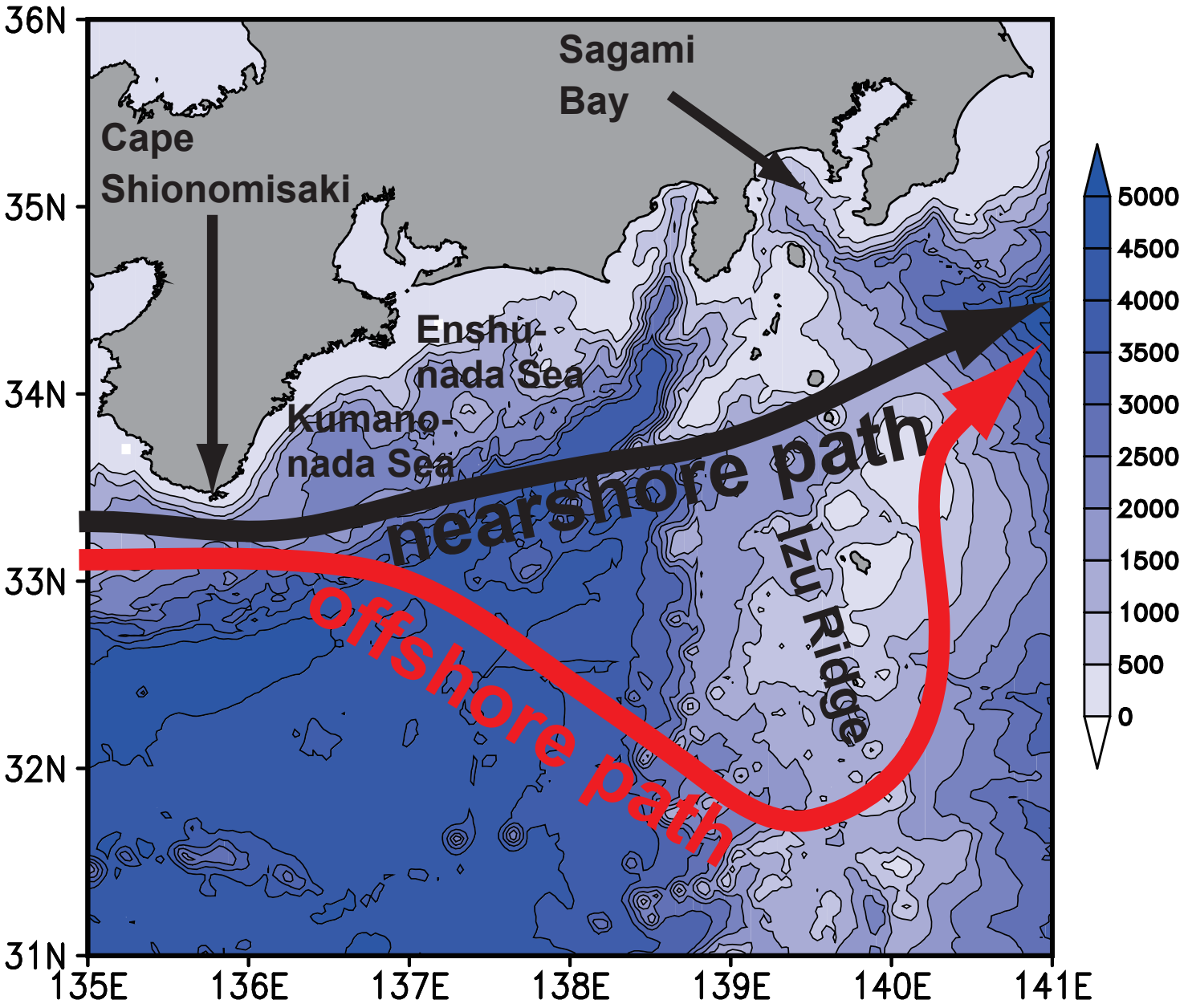
36N
35N
34N
33N
32N
31N
135E
136E
137E
138E
139E
140E
141E
Sagami
Bay
Cape
Shionomisaki
Enshu-
nada Sea
Kumano-
nada Sea
nearshore path
offshore path
Izu Ridge
5000
4500
4000
3500
3000
2500
2000
1500
1000
500
0

Fig. 1

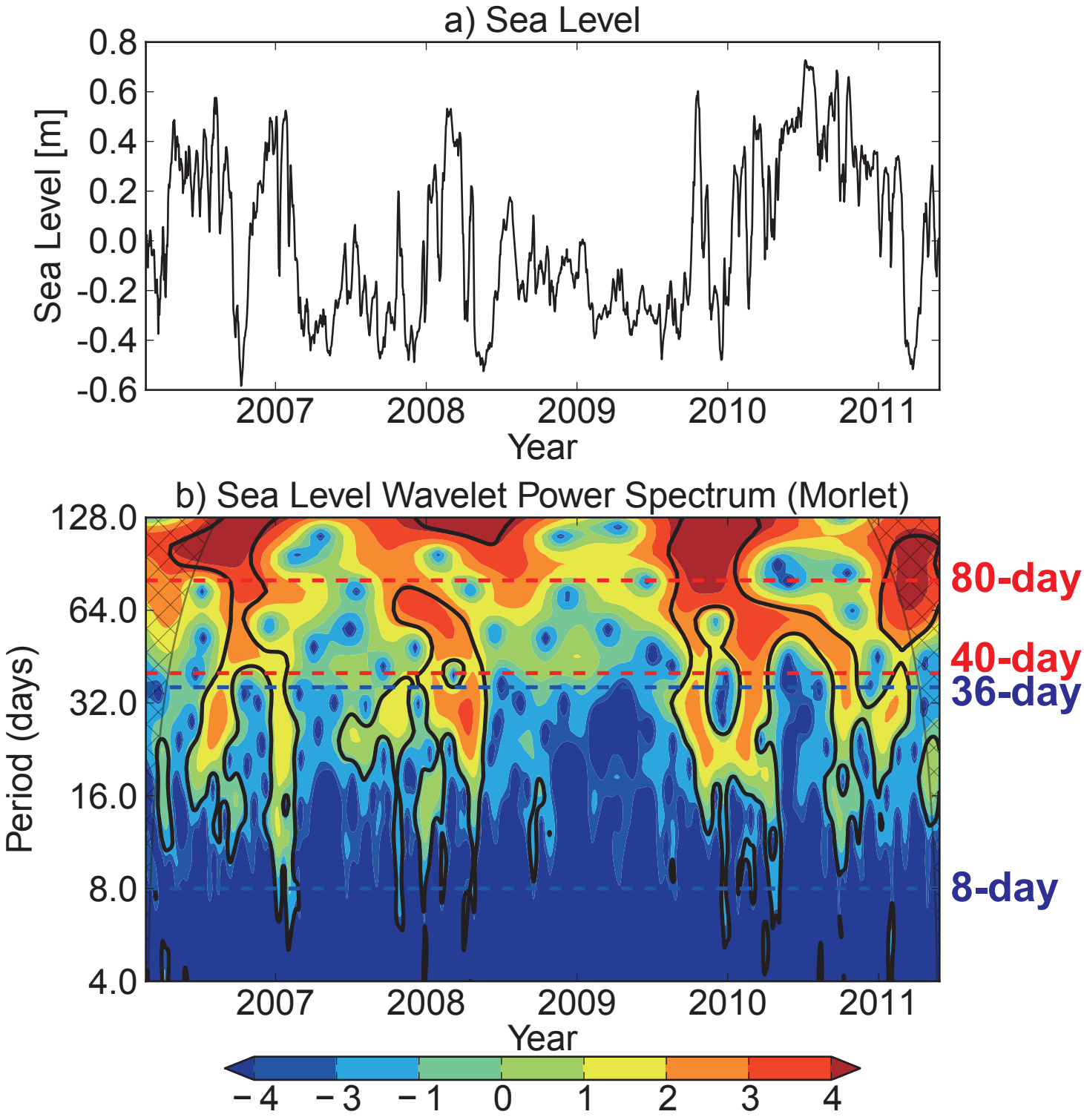
a) Sea Level
Sea Level [m]
0.8
0.6
0.4
0.2
0.0
-0.2
-0.4
-0.6
2007
2008
2009
2010
2011
Year
b) Sea Level Wavelet Power Spectrum (Morlet)
Period (days)
128.0
64.0
32.0
16.0
8.0
4.0
80-day
40-day
36-day
8-day
2007
2008
2009
2010
2011
Year
−4
−3
−1
0
1
2
3
4

Fig. 2

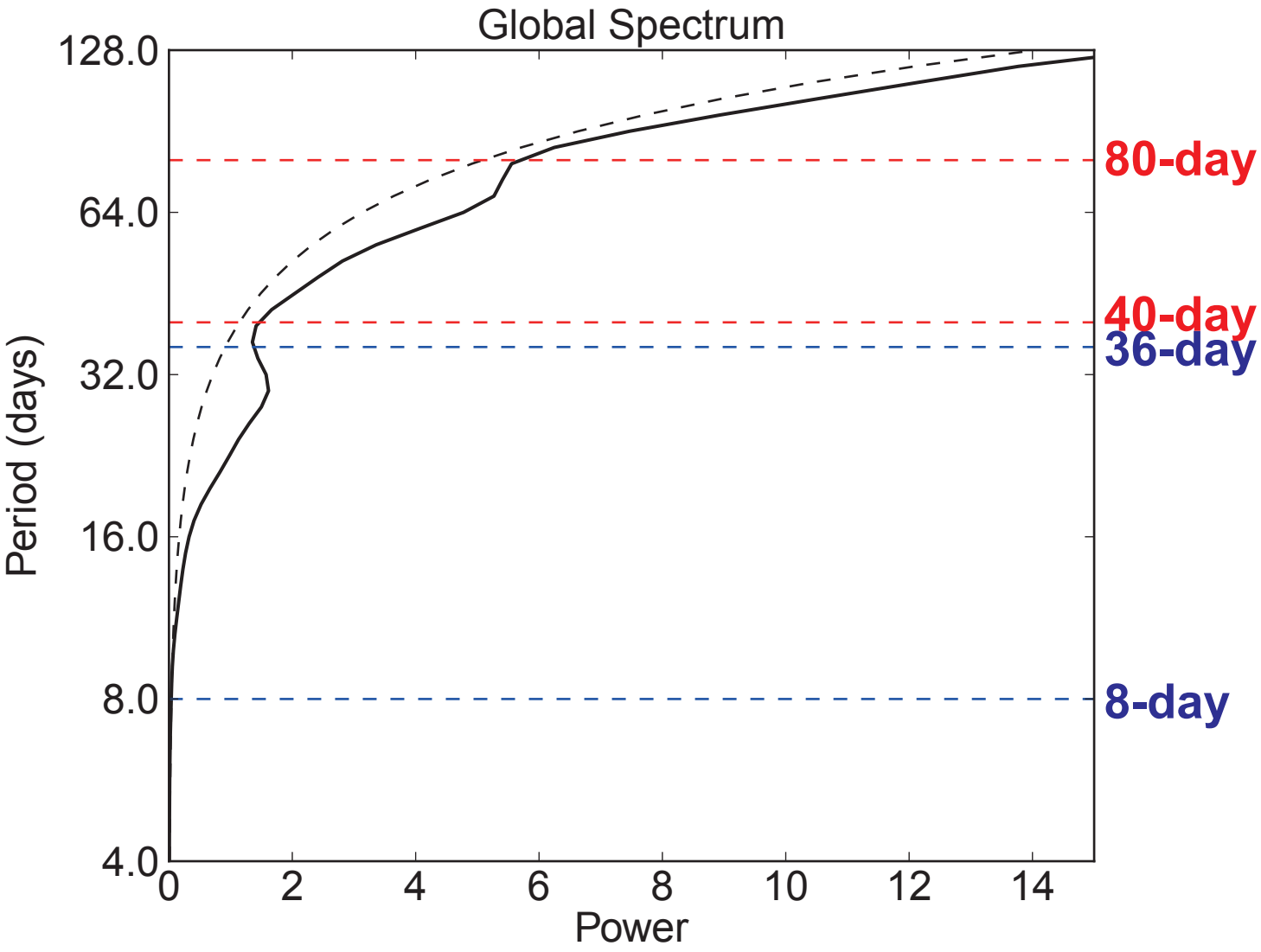
Global Spectrum
128.0
64.0
32.0
16.0
8.0
4.0
Period (days)
0
2
4
6
8
10
12
14
Power
80-day
40-day
36-day
8-day

Fig. 3

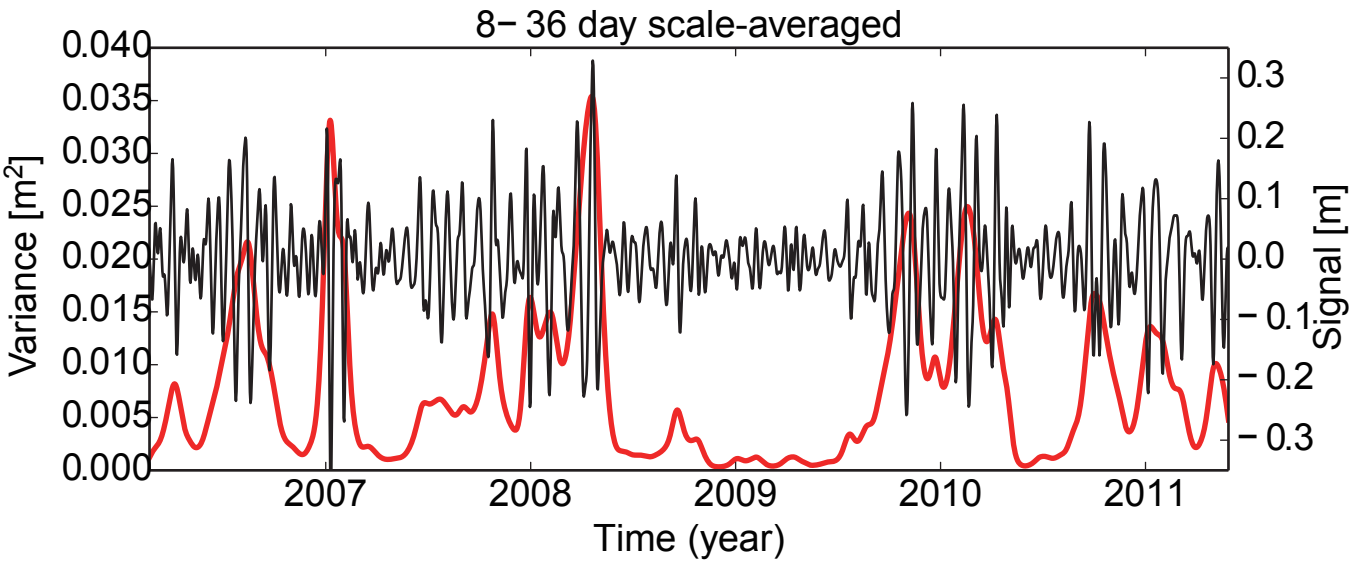
8− 36 day scale-averaged
Variance [m²]
Signal [m]
Time (year)
0.040
0.035
0.030
0.025
0.020
0.015
0.010
0.005
0.000
0.3
0.2
0.1
0.0
− 0.1
− 0.2
− 0.3
2007
2008
2009
2010
2011

Fig. 4

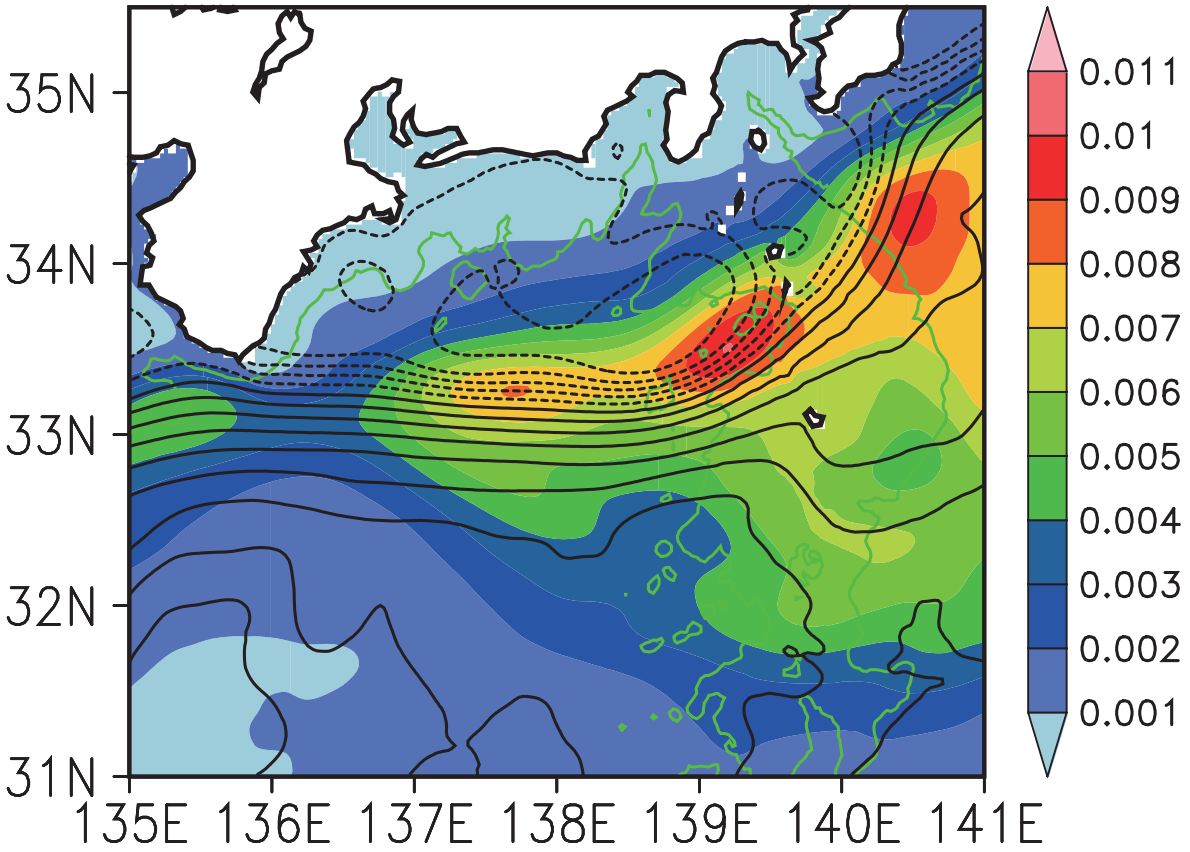
35N
34N
33N
32N
31N
135E
136E
137E
138E
139E
140E
141E
0.011
0.01
0.009
0.008
0.007
0.006
0.005
0.004
0.003
0.002
0.001

Fig. 5

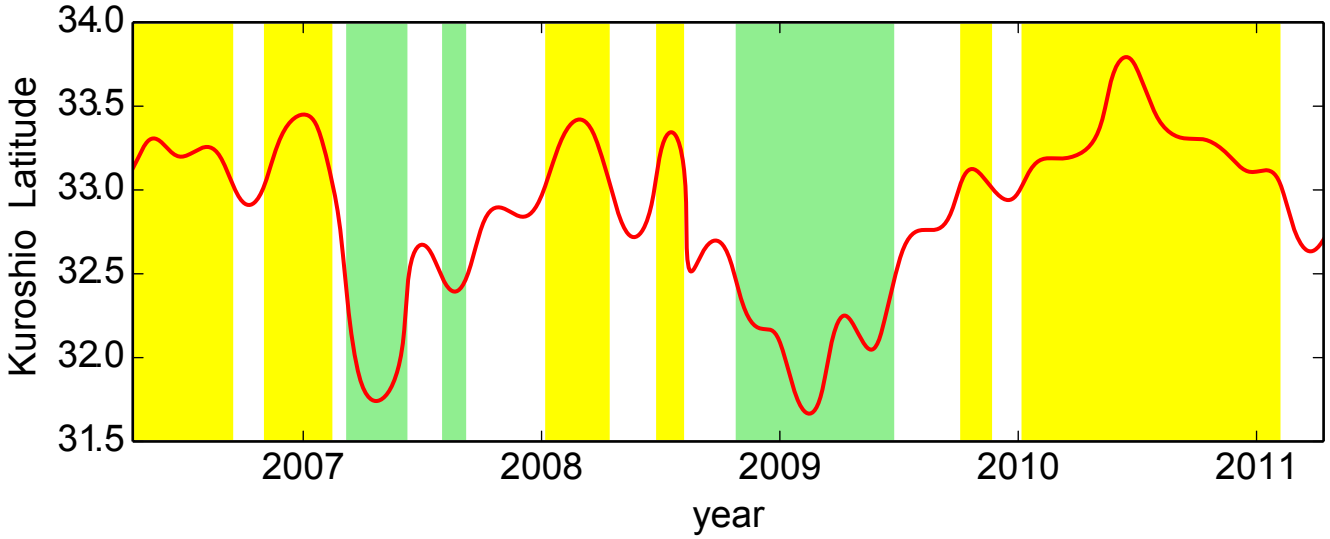
34.0
33.5
33.0
32.5
32.0
31.5
Kuroshio Latitude
2007
2008
2009
2010
2011
year

Fig. 6

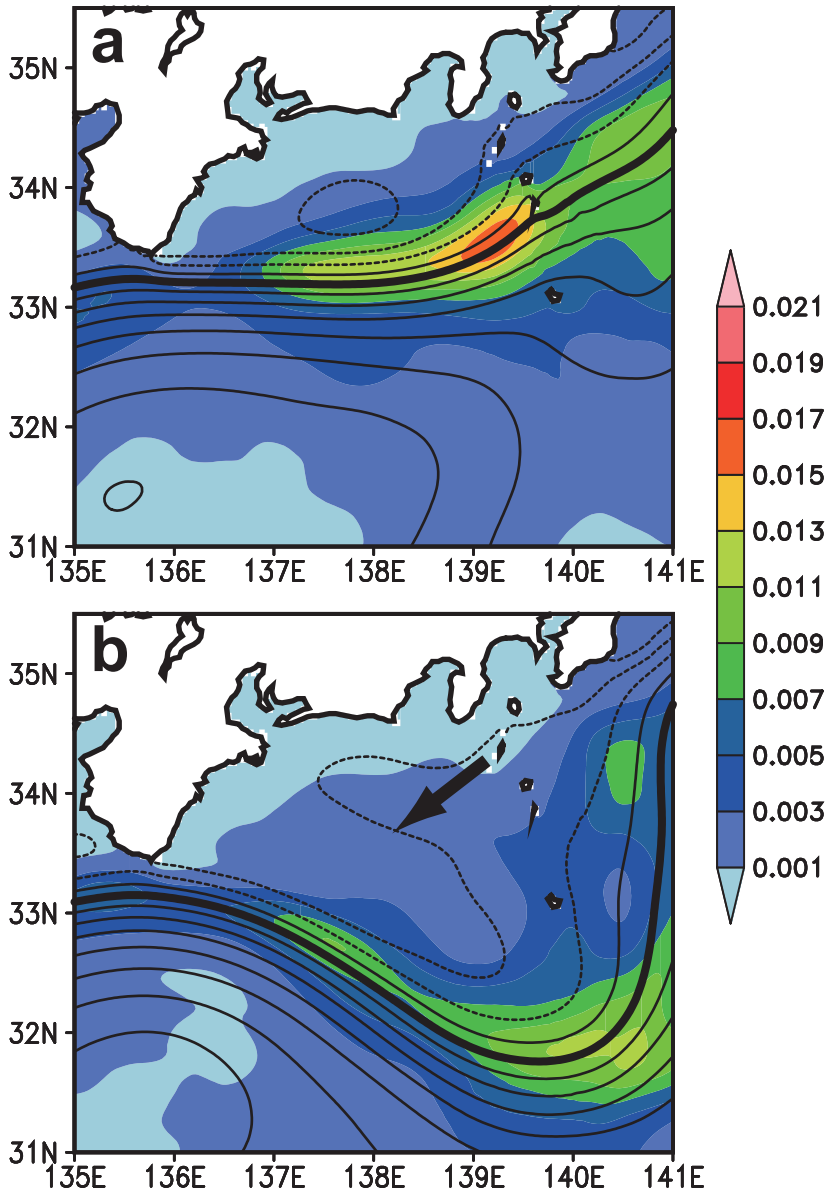
a
b
35N
34N
33N
32N
31N
135E
136E
137E
138E
139E
140E
141E
0.021
0.019
0.017
0.015
0.013
0.011
0.009
0.007
0.005
0.003
0.001

Fig. 7

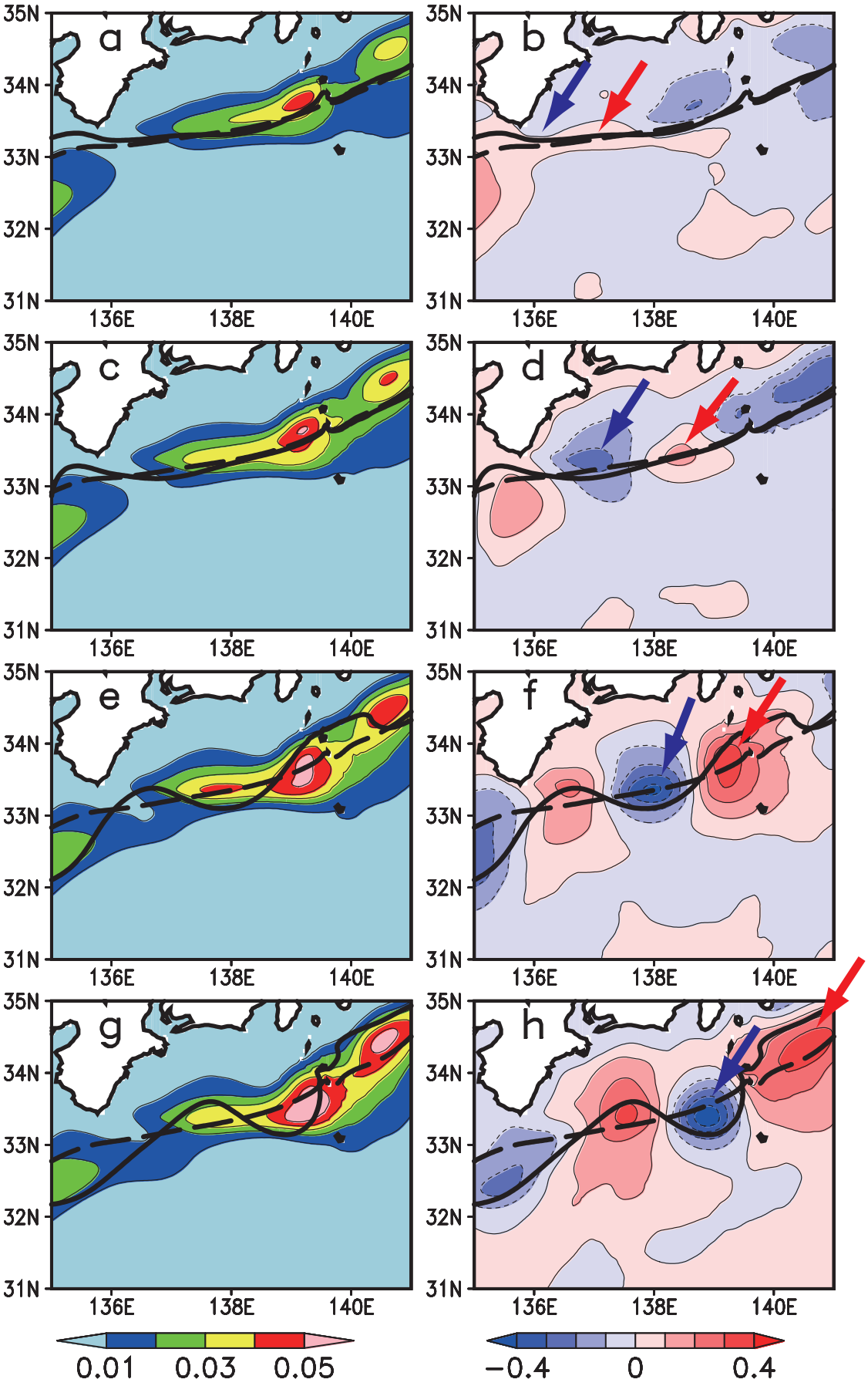

Fig. 8

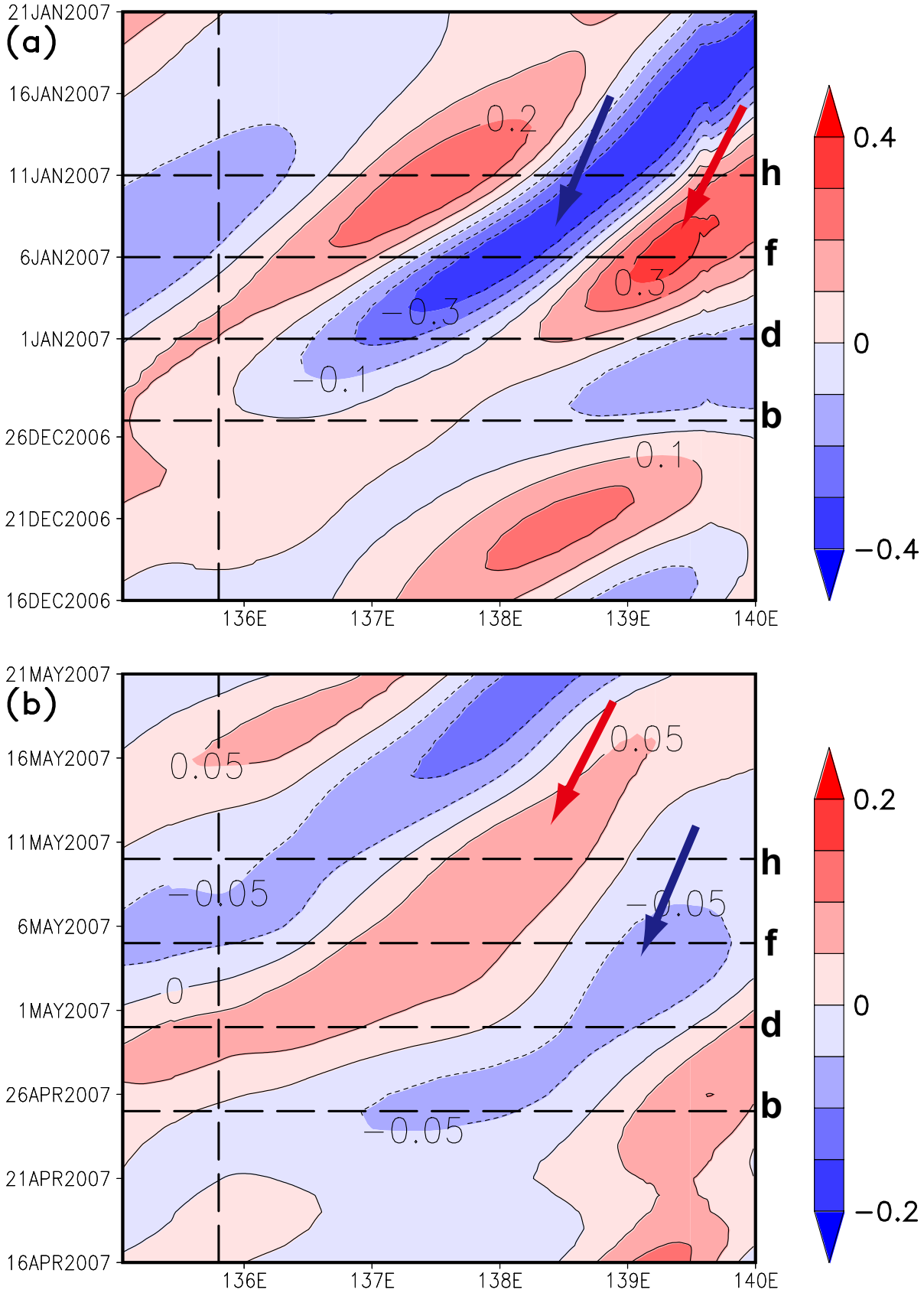
(a)
21JAN2007
16JAN2007
11JAN2007
6JAN2007
1JAN2007
26DEC2006
21DEC2006
16DEC2006
136E
137E
138E
139E
140E
h
f
d
b
0.2
0.3
−0.3
−0.1
0.1
0.4
0
−0.4
(b)
21MAY2007
16MAY2007
11MAY2007
6MAY2007
1MAY2007
26APR2007
21APR2007
16APR2007
136E
137E
138E
139E
140E
h
f
d
b
0.05
−0.05
0
−0.05
0.05
0.2
0
−0.2

Fig. 9

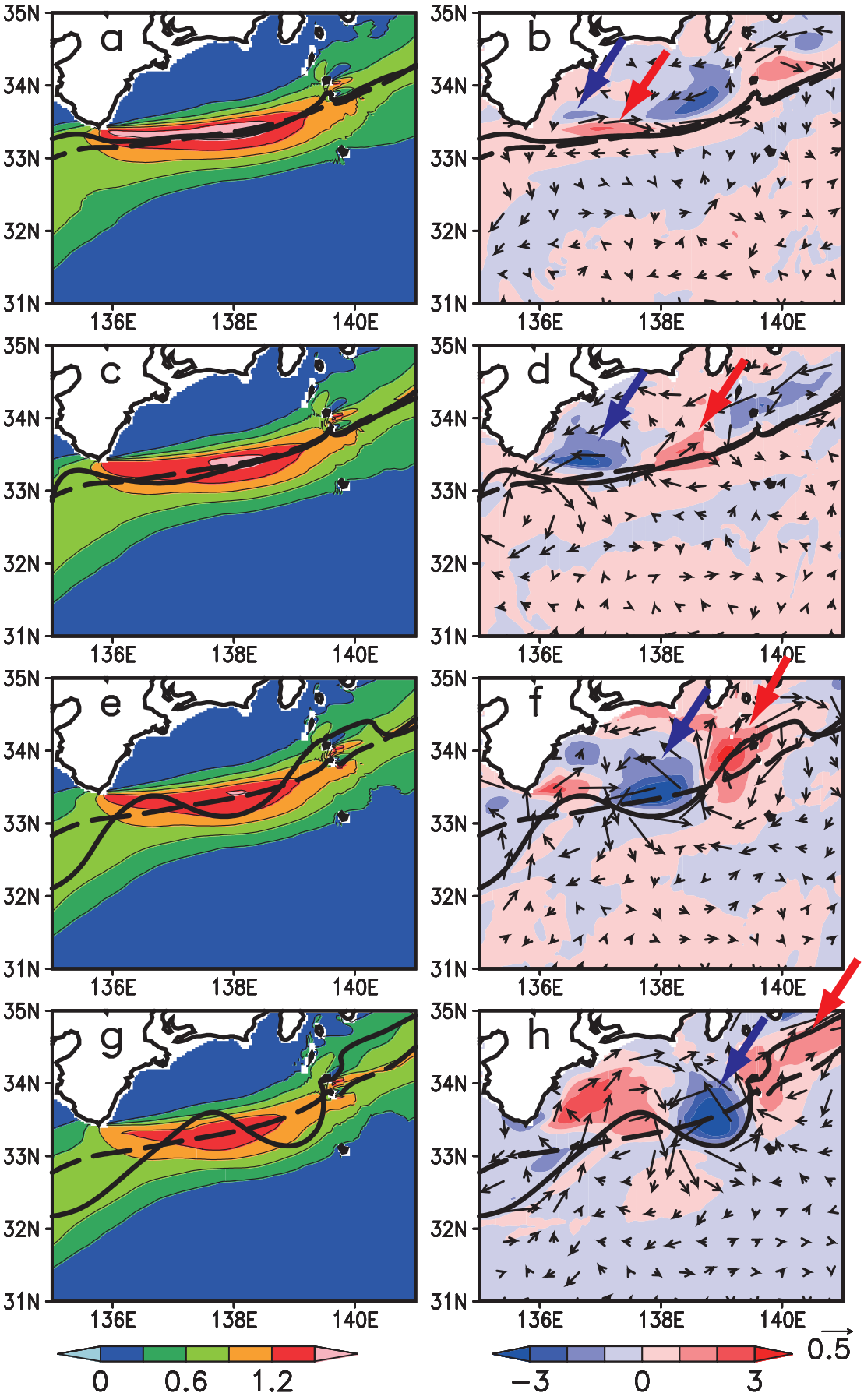

Fig. 10

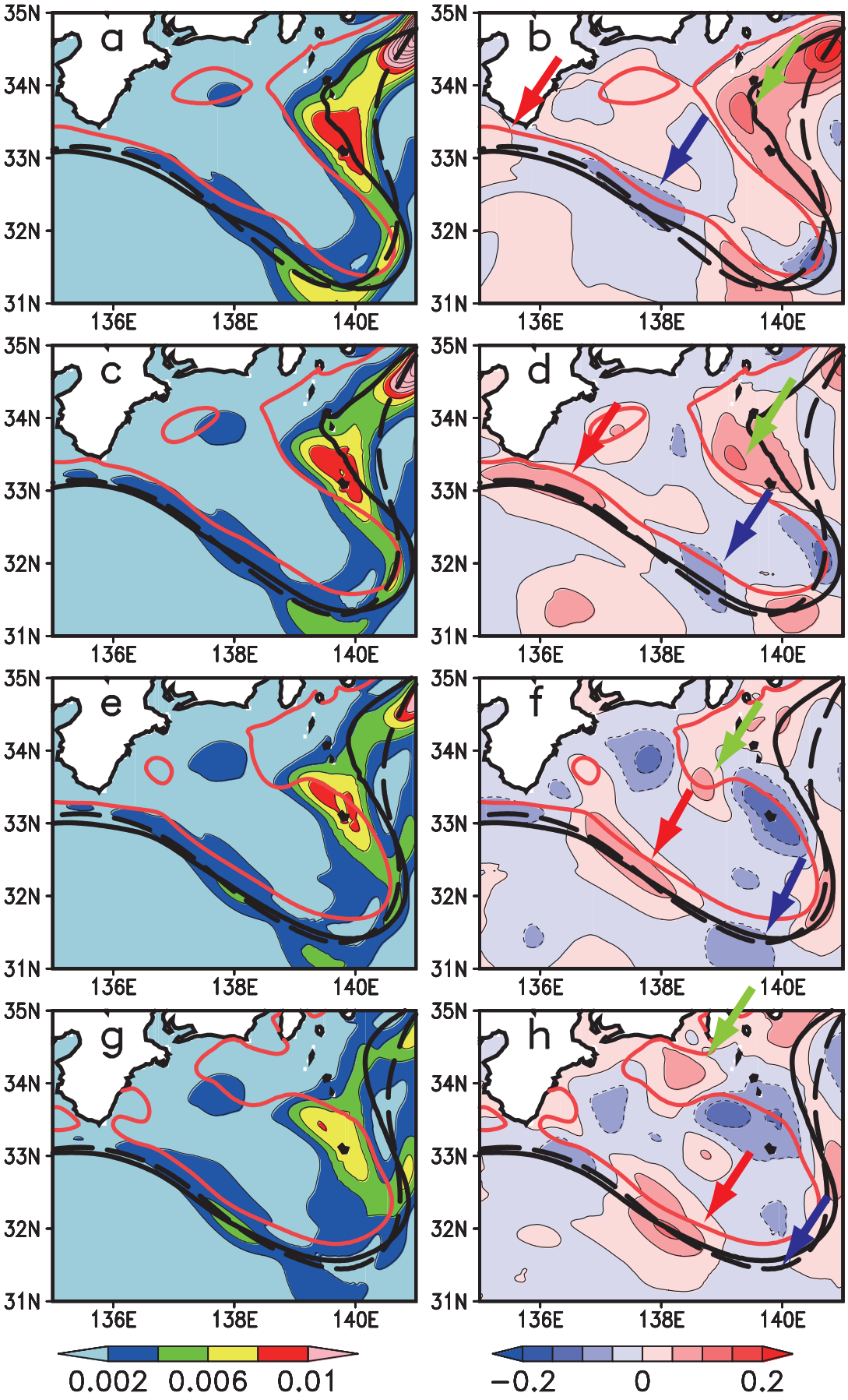
a
b
c
d
e
f
g
h
35N
34N
33N
32N
31N
136E
138E
140E
0.002
0.006
0.01
−0.2
0
0.2

Fig. 11

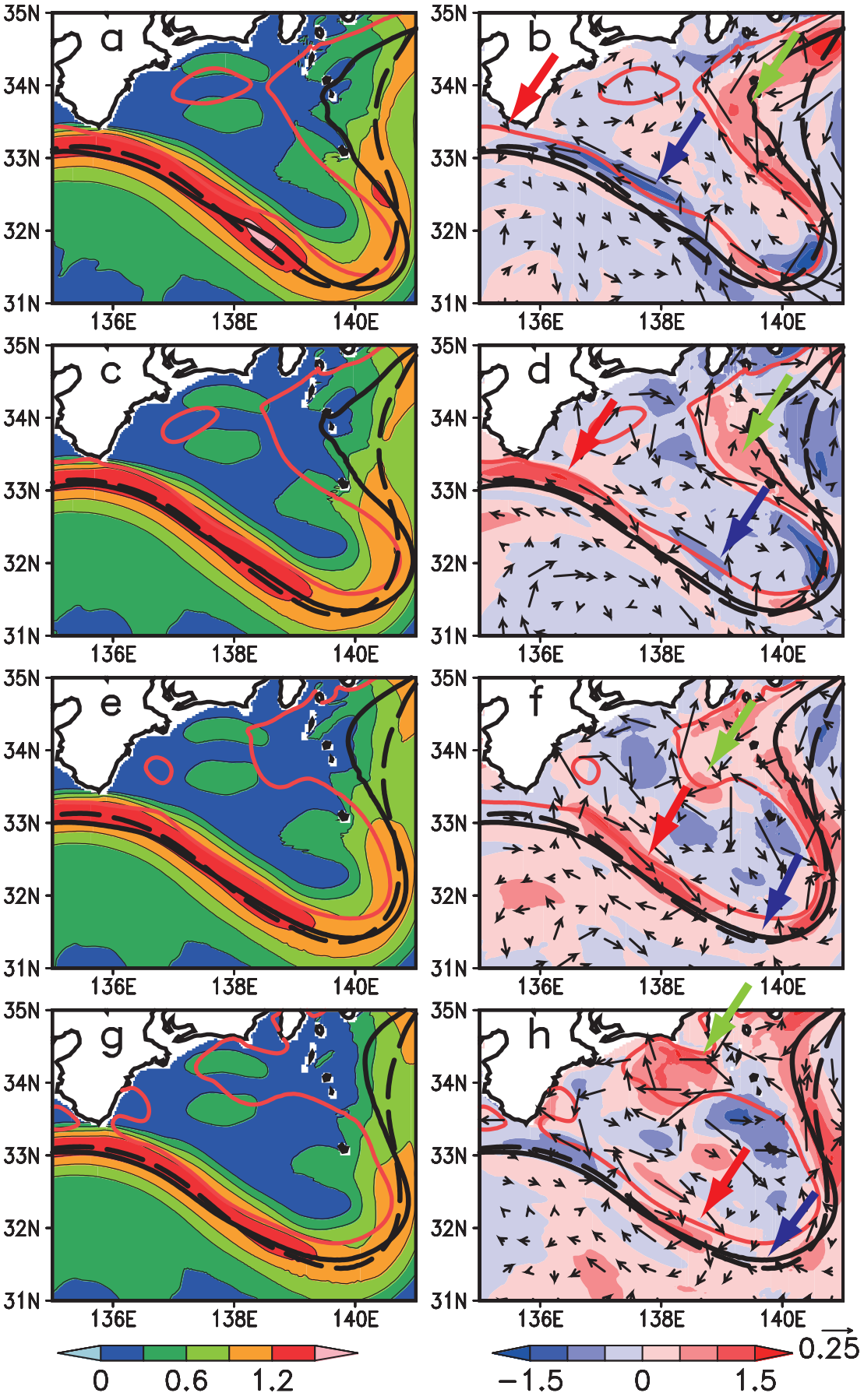

Fig. 12

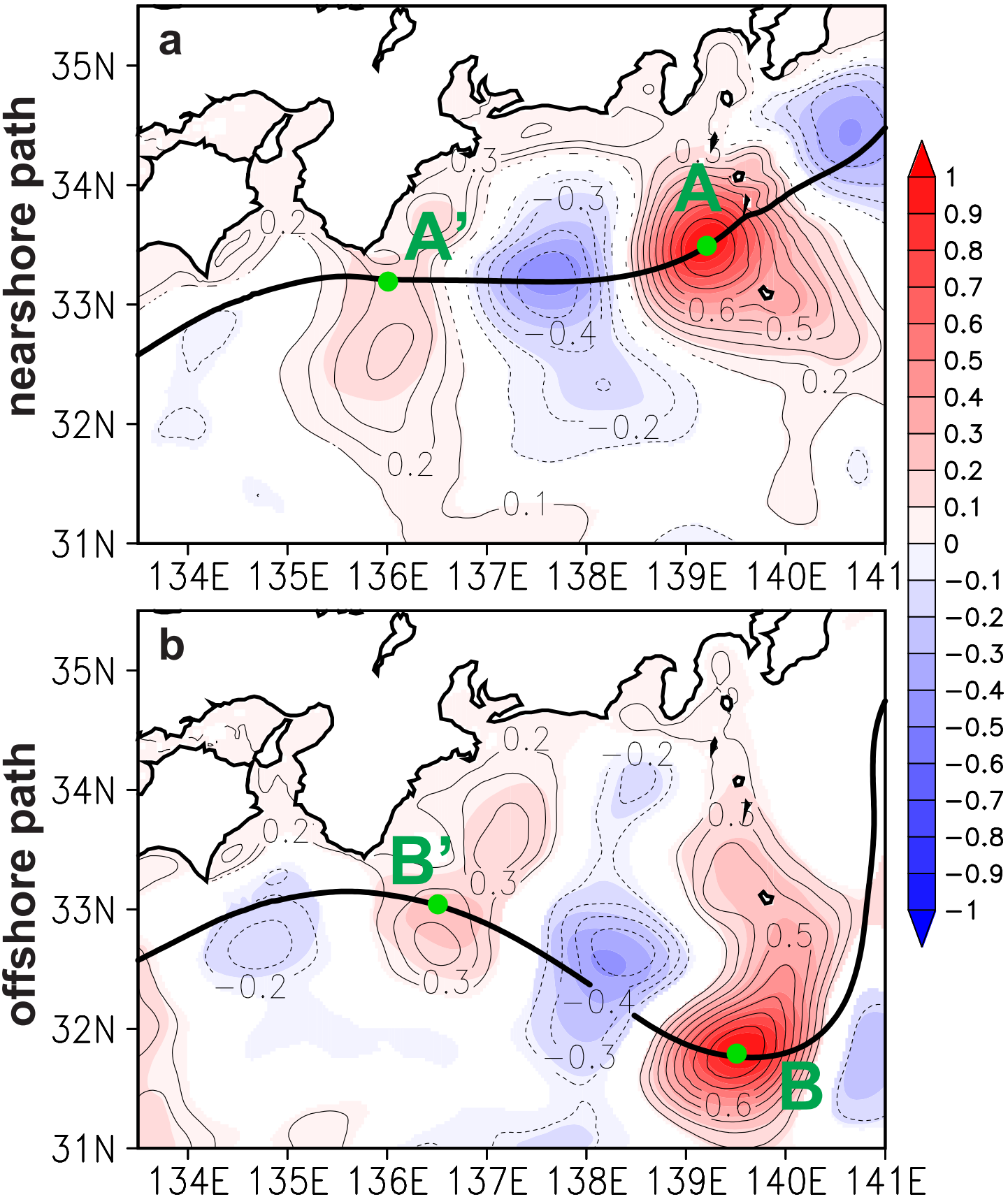
a
b
nearshore path
offshore path
35N
34N
33N
32N
31N
134E
135E
136E
137E
138E
139E
140E
141
141E
A
A'
B
B'
1
0.9
0.8
0.7
0.6
0.5
0.4
0.3
0.2
0.1
0
−0.1
−0.2
−0.3
−0.4
−0.5
−0.6
−0.7
−0.8
−0.9
−1

Fig. 13

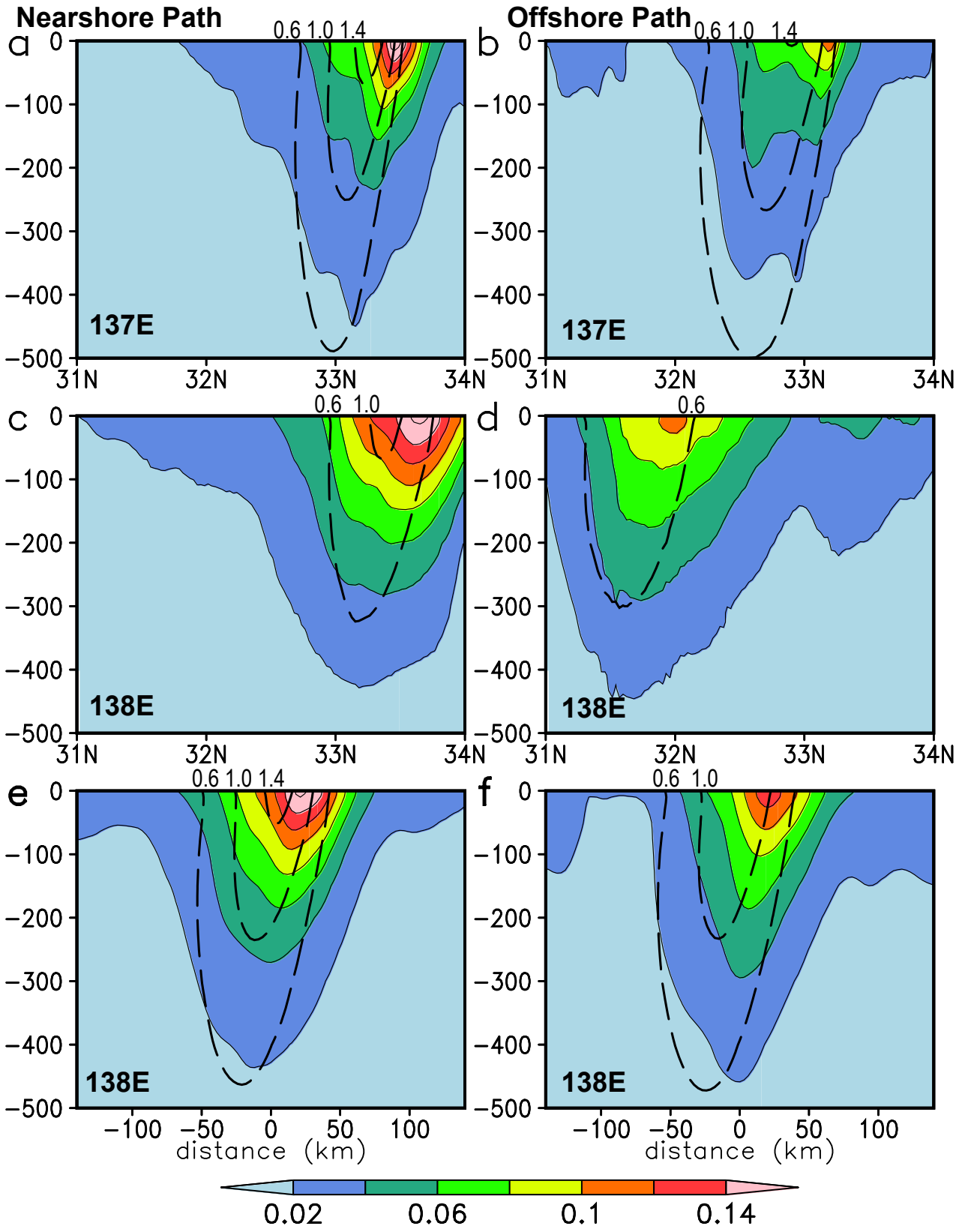
Nearshore Path
Offshore Path
a
b
c
d
e
f
0.6 1.0 1.4
0.6 1.0
0.6
137E
138E
0
−100
−200
−300
−400
−500
31N
32N
33N
34N
−100 −50 0 50 100
distance (km)
0.02
0.06
0.1
0.14

Fig. 14

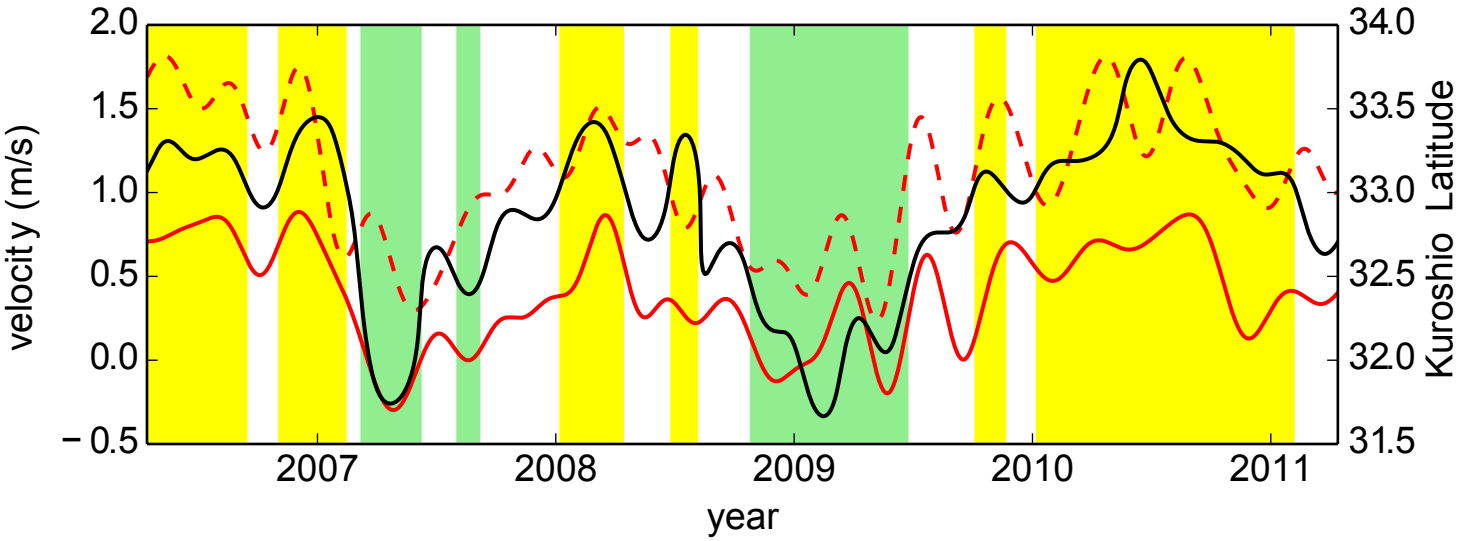
2.0
1.5
1.0
0.5
0.0
− 0.5
velocity (m/s)
34.0
33.5
33.0
32.5
32.0
31.5
Kuroshio Latitude
2007
2008
2009
2010
2011
year

Fig. 15

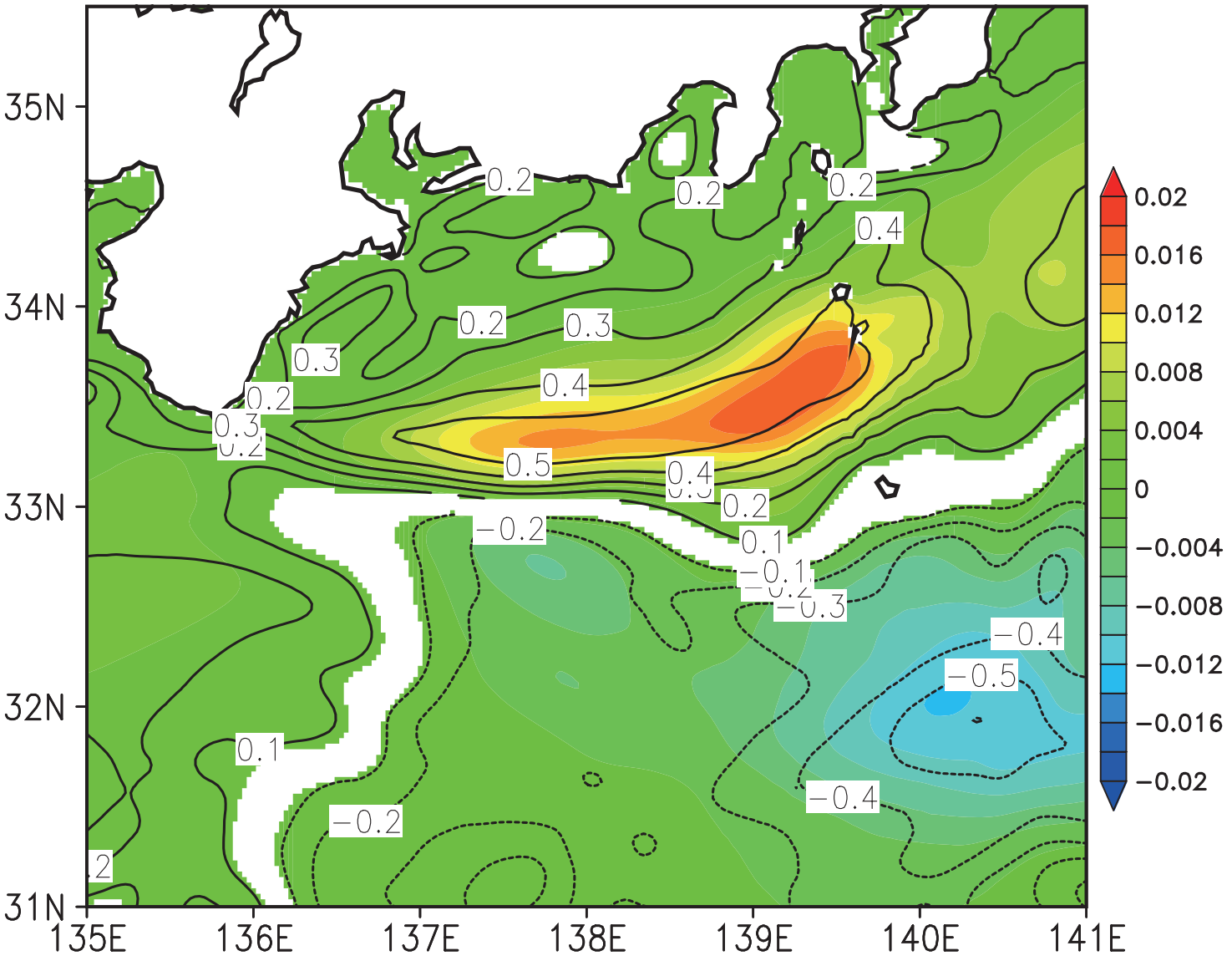
35N
34N
33N
32N
31N
135E
136E
137E
138E
139E
140E
141E
0.2
0.3
0.4
0.5
0.1
−0.1
−0.2
−0.3
−0.4
−0.5
0.02
0.016
0.012
0.008
0.004
0
−0.004
−0.008
−0.012
−0.016
−0.02

Fig. 16

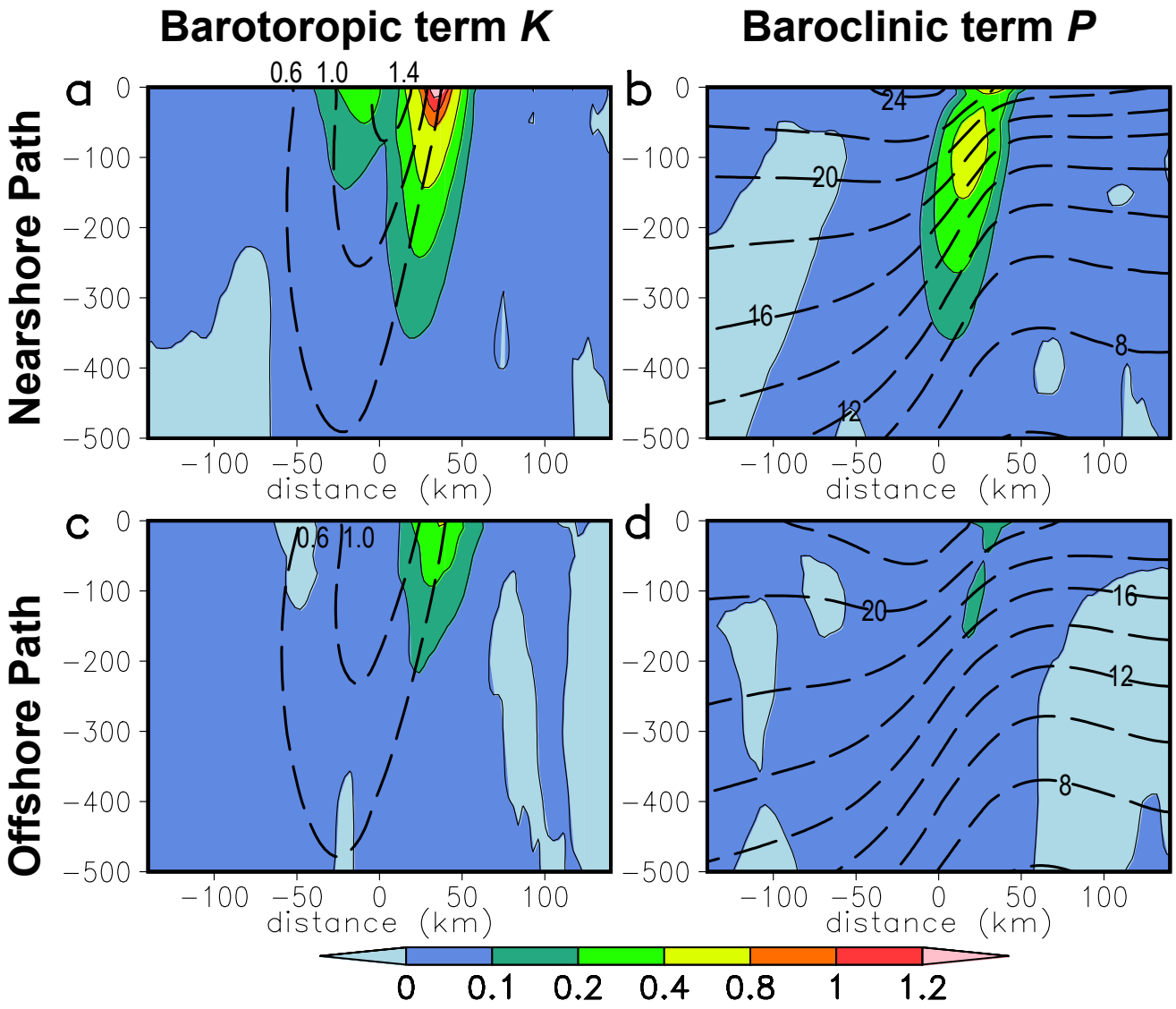
Barotoropic term K
Baroclinic term P
Nearshore Path
Offshore Path
a
b
c
d
0.6 1.0 1.4
24
20
16
12
8
0.6 1.0
0 −100 −200 −300 −400 −500
−100 −50 0 50 100
distance (km)
0 0.1 0.2 0.4 0.8 1 1.2

Fig. 17

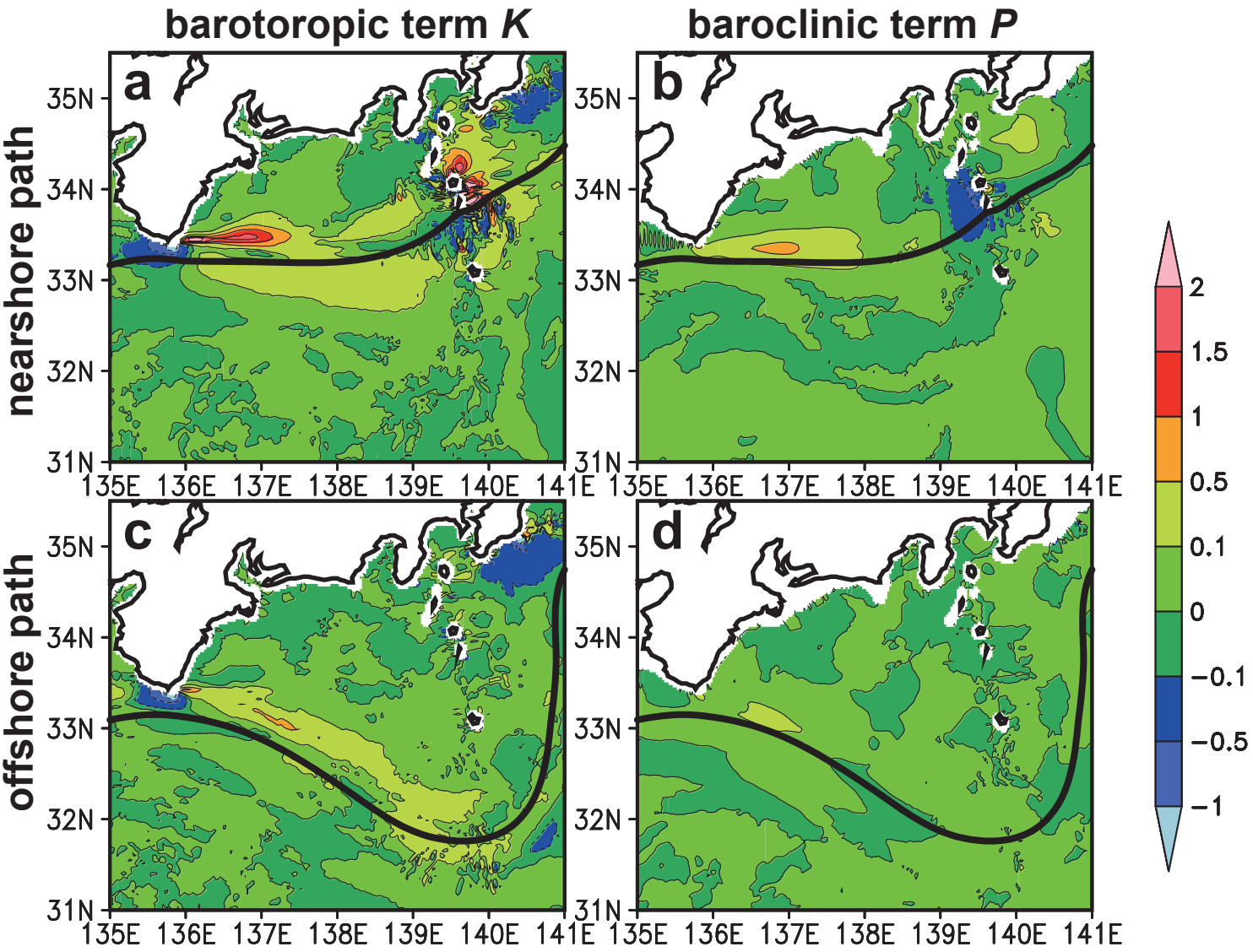
barotoropic term K
baroclinic term P
nearshore path
offshore path
a
b
c
d
35N
34N
33N
32N
31N
135E 136E 137E 138E 139E 140E 141E
2
1.5
1
0.5
0.1
0
−0.1
−0.5
−1

Fig. 18

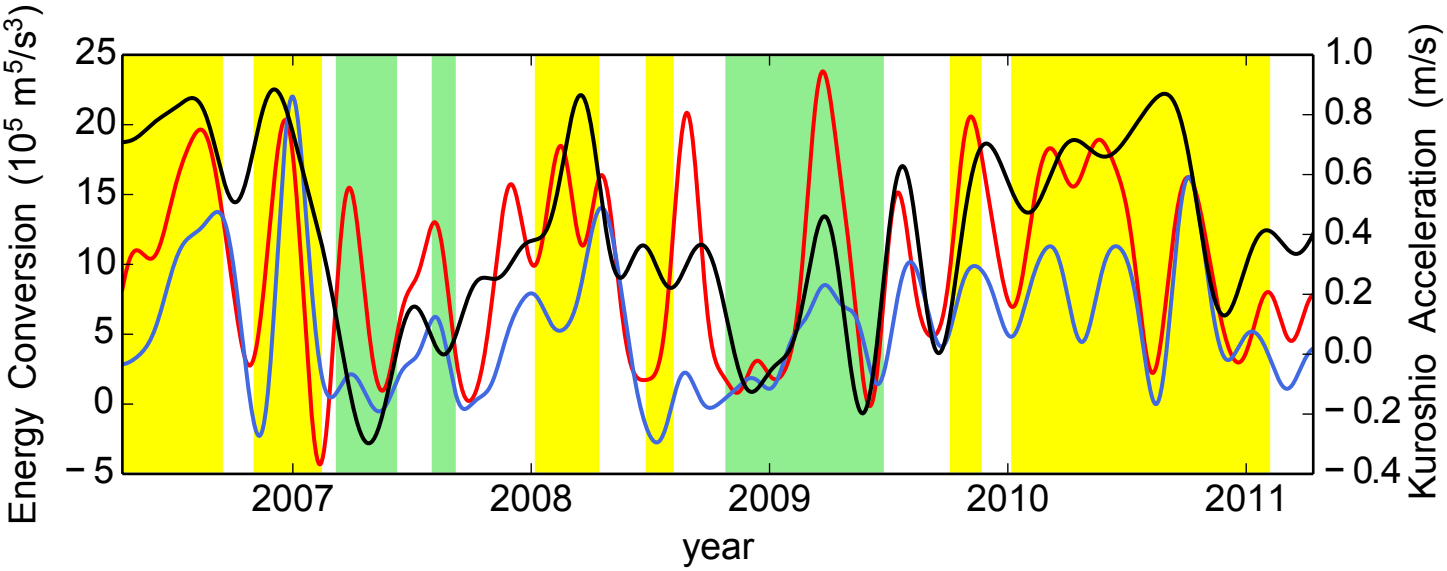
Energy Conversion (10^5 m^5/s^3)
25
20
15
10
5
0
−5
2007
2008
2009
2010
2011
year
1.0
0.8
0.6
0.4
0.2
0.0
−0.2
−0.4
Kuroshio Acceleration (m/s)

Fig. 19

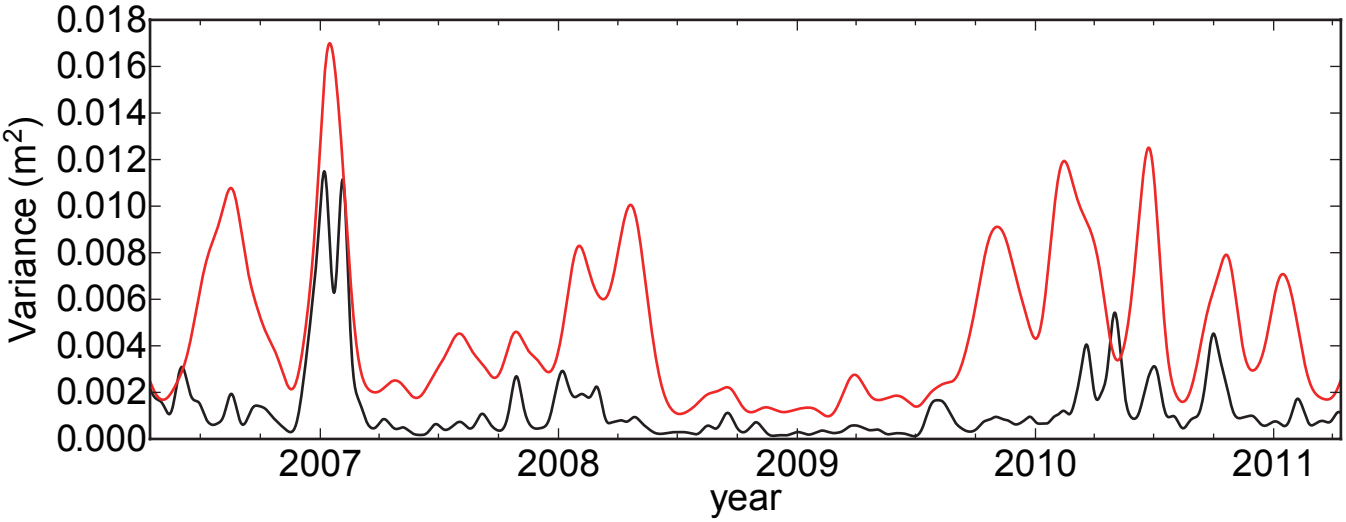
0.018
0.016
0.014
0.012
0.010
0.008
0.006
0.004
0.002
0.000
Variance (m²)
2007
2008
2009
2010
2011
year

Fig. 20

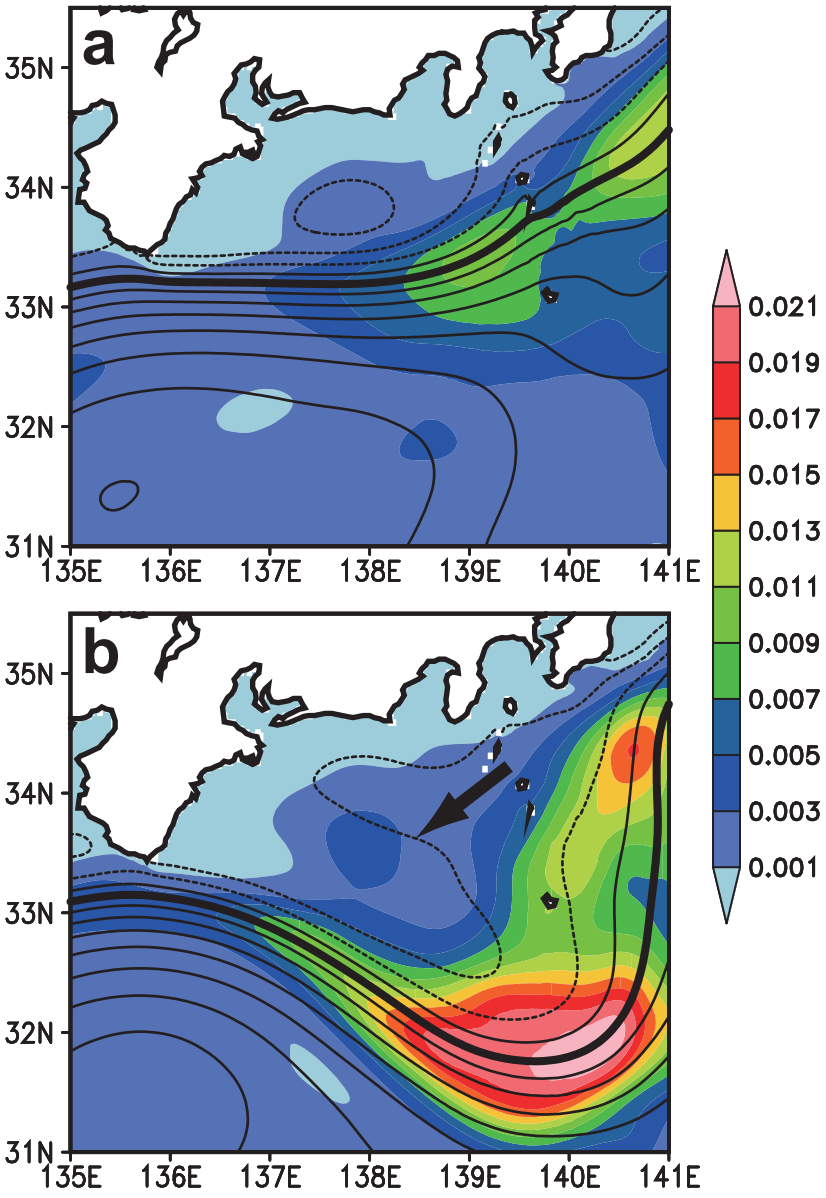
a
b
35N
34N
33N
32N
31N
135E
136E
137E
138E
139E
140E
141E
0.021
0.019
0.017
0.015
0.013
0.011
0.009
0.007
0.005
0.003
0.001

Fig. 21

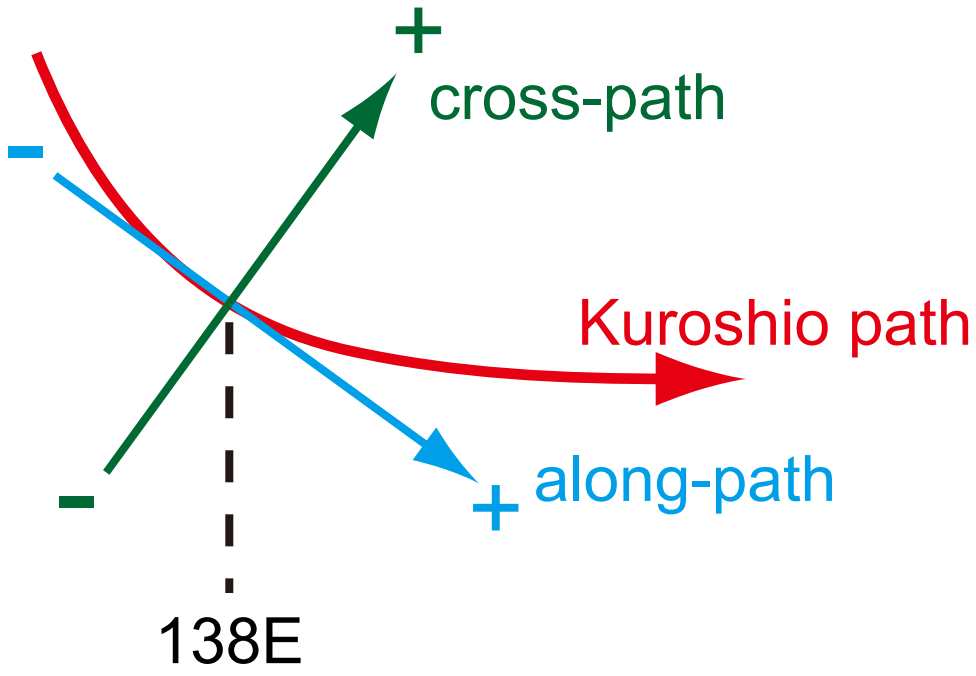

Fig. 22